ANNUAL REVIEWS

Annual Review of Chemical and Biomolecular Engineering

Polymer-Infiltrated Nanoparticle Films Using Capillarity-Based Techniques: Toward Multifunctional Coatings and Membranes

R. Bharath Venkatesh,[1] Neha Manohar,[1] Yiwei Qiang,[2] Haonan Wang,[3] Hong Huy Tran,[1,4] Baekmin Q. Kim,[1,5] Anastasia Neuman,[1] Tian Ren,[1] Zahra Fakhraai,[3] Robert A. Riggleman,[1] Kathleen J. Stebe,[1] Kevin Turner,[6] and Daeyeon Lee[1,*]

[1]Department of Chemical and Biomolecular Engineering, University of Pennsylvania, Philadelphia, Pennsylvania 19104, USA; email: rbharath@seas.upenn.edu, nmanohar@seas.upenn.edu, annaneu@seas.upenn.edu, tianr@seas.upenn.edu, rrig@seas.upenn.edu, kstebe@seas.upenn.edu, daeyeon@seas.upenn.edu

[2]Department of Materials Science and Engineering, University of Pennsylvania, Philadelphia, Pennsylvania 19104, USA; email: yiweiq@seas.upenn.edu

[3]Department of Chemistry, University of Pennsylvania, Philadelphia, Pennsylvania 19104, USA; email: whaonan@seas.upenn.edu, fakhraai@seas.upenn.edu

[4]Université Grenoble Alpes, CNRS, Grenoble INP (Institute of Engineering, Université Grenoble Alpes), LMGP, 38000 Grenoble, France; email: hong-huy.tran@grenoble-inp.fr

[5]Department of Chemical and Biomolecular Engineering and KAIST Institute for the NanoCentury, Korea Advanced Institute of Science and Technology (KAIST), Daejeon 34141, Korea; email: baekmin@seas.upenn.edu

[6]Department of Mechanical Engineering and Applied Mechanics, University of Pennsylvania, Philadelphia, Pennsylvania 19104, USA; email: kturner@seas.upenn.edu

Annu. Rev. Chem. Biomol. Eng. 2021. 12:411–37

The *Annual Review of Chemical and Biomolecular Engineering* is online at chembioeng.annualreviews.org

https://doi.org/10.1146/annurev-chembioeng-101220-093836

*Corresponding author

Keywords

nanocomposites, infiltration, capillarity, nanoparticle packings, confinement, cross-functional properties

Abstract

Polymer-infiltrated nanoparticle films (PINFs) are a new class of nanocomposites that offer synergistic properties and functionality derived from unusually high fractions of nanomaterials. Recently, two versatile techniques,

capillary rise infiltration (CaRI) and solvent-driven infiltration of polymer (SIP), have been introduced that exploit capillary forces in films of densely packed nanoparticles. In CaRI, a highly loaded PINF is produced by thermally induced wicking of polymer melt into the nanoparticle packing pores. In SIP, exposure of a polymer–nanoparticle bilayer to solvent vapor atmosphere induces capillary condensation of solvent in the pores of nanoparticle packing, leading to infiltration of polymer into the solvent-filled pores. CaRI/SIP PINFs show superior properties compared with polymer nanocomposite films made using traditional methods, including superb mechanical properties, thermal stability, heat transfer, and optical properties. This review discusses fundamental aspects of the infiltration process and highlights potential applications in separations, structural coatings, and polymer upcycling—a process to convert polymer wastes into useful chemicals.

1. INTRODUCTION

Polymer nanocomposite films have found myriad applications as coatings and membranes because of their useful and unique properties that derive from the functionality of nanoscale materials and the processability and flexibility of polymers. Numerous studies have demonstrated the superb mechanical (1, 2), barrier, electrical, and optical (3–5) properties offered by polymer nanocomposite coatings and membranes. For example, composite coatings prepared by layer-by-layer assembly of a flame-retardant nanofiller, such as clay platelets, and an oppositely charged polyelectrolyte have excellent intumescent properties, protecting the coated materials against fire damage (6–10). Nanocomposite membranes can be used in gas separation (11) and as reverse osmosis membranes (12) that confer both high selectivity and high permeability, as well as in packaging to meet specific barrier property requirements (13, 14). Conductive and catalytic nanocomposite films and coatings display increased cyclic lifetimes and mechanical stability, making them ideal components (e.g., as electrodes) in energy conversion and storage applications (15), including high-efficiency solar cells (16, 17) and batteries. Finally, given their enhanced response to external stimuli, polymer nanocomposite films also have been investigated for sensing technologies (18, 19).

Highly loaded polymer nanocomposite films, which we define as those with a nanoparticle volume fraction of greater than 50%, have additional property enhancements over their counterparts. Thermal and electrical percolation, which is necessary to achieve high conductivity, occurs with high filler contents (20). Thus, highly loaded polymer nanocomposites display orders-of-magnitude enhancement in conductivity (14). Higher filler content also confers higher refractive indices (21) and enhancement of both mechanical strength and toughness (22, 23). For example, nanocomposite films with a high filler fraction of anisotropic nanoparticles that mimic the structure of nacre can exhibit high strength, stiffness, and toughness simultaneously (24, 25), making them uniquely suited for protective coating applications.

Traditional methods for producing polymer nanocomposites present several challenges in manufacturing nanocomposite coatings and membranes with extremely high nanoparticle fractions. In general, the strong interparticle forces and high surface area of nanoscale materials make them prone to aggregation, making mixing, compounding, and thin film drawing very challenging. Conventional solution or melt-based methods (26–29) are typically optimized for processing mixtures with less than 10 vol% of nanoparticles. In situ polymerization (30), which entails mixing monomers and nanoparticles and subsequently polymerizing the monomers in the interstices of the nanoparticles, allows for higher fill fractions owing to the low viscosity of monomers. However, nanoparticles may inhibit polymerization, and many natural polymers, such as polysaccharides and proteins, cannot be easily polymerized from their monomers. Layer-by-layer assembly (31, 32) of oppositely charged nanoparticles and polymers can create highly filled composites with uniform

filler distributions but can be time-consuming and is typically limited to water-soluble species of opposite charge.

To circumvent these hurdles, polymer infiltration into the interstices of packed nanoparticle films is an intriguing alternative approach to create highly filled nanocomposite films with a wide variety of polymers and nanoparticles. Representative methods of polymer infiltration include vacuum-assisted infiltration (33, 34), in situ electropolymerization (35), and initiated chemical vapor deposition (36). Shear pressing (37) has also displayed potential to produce high filler percentage composites with controlled orientations.

Recently, facile and potentially scalable methods to manufacture polymer-infiltrated nanoparticle films (PINFs) without any sophisticated instruments and equipment have been developed using capillarity-based phenomena (38). Capillary rise infiltration (CaRI) involves preparing a two-layer film composed of a polymer layer and a nanoparticle layer and then heating this bilayer above the glass transition temperature (T_g) of the polymer to induce polymer infiltration. The polymer wicks into the interstices of the nanoparticle layer via capillary action. By controlling the thickness of the polymer layer relative to that of the nanoparticle layer, PINFs with graded or uniform porosity can be created with ease (39). This method can be further expanded to enable patterning of PINFs by inducing CaRI of a low-T_g polymer from a swollen network (40). In a second method, solvent-driven infiltration of polymer (SIP), capillary condensation is exploited to induce polymer infiltration into nanoparticle films (30, 41–43). A bilayer similar to that used in the CaRI method is exposed to solvent vapor, which condenses in the voids of the nanoparticle packing via capillary condensation. The condensed solvent diffuses into and plasticizes the underlying polymer layer, inducing polymer infiltration into the liquid-filled interstices of the nanoparticle film.

Both CaRI and SIP are relatively simple, scalable techniques that enable the fabrication of PINFs with a wide range of polymers and nanoparticles. In addition to providing versatile means for PINF preparation, CaRI and SIP also present unique opportunities to study the transport and thermodynamic phenomena of extremely confined polymers. This review highlights new discoveries and understanding of these fundamental aspects related to CaRI and SIP processes and also discusses unique functionality and properties that have been derived from PINFs made using these methods. We conclude with an outlook on future studies to further enhance our understanding of polymer infiltration phenomena in CaRI and SIP and propose several new areas of applications for which CaRI and SIP coatings and membranes are particularly well suited.

2. CAPILLARY RISE INFILTRATION

2.1. Capillary Rise Infiltration of Polymer into Nanoparticle Packing

CaRI is a simple yet powerful method to fabricate PINFs (see the sidebar titled Capillarity Basics). In CaRI, a bilayer of packed nanoparticles and a polymer is prepared via various film deposition techniques, including spin, blade, dip, and spray coating. Typically, a polymer film is formed on a substrate, and a packing of nanoparticles is produced atop the polymer layer. Alternatively, an inverted bilayer can be prepared by first creating a nanoparticle film and then placing a polymer layer atop the nanoparticle layer either by directly using a solution deposition technique (e.g., spin coating) or by placing a freestanding polymer layer. If a solution-based technique is used to prepare a polymer layer atop a nanoparticle layer, the interstices between nanoparticles become partially filled with polymer during the coating process; subsequent heat treatment leads to complete filling of the interstices of the nanoparticle packing via CaRI. In preparing a bilayer structure, it is important to use a solvent that does not compromise the integrity of the first layer when depositing the second layer. To protect the first layer and to facilitate the deposition of the second layer, a

CAPILLARITY BASICS

Capillarity-based phenomena are induced by the action of deformable interfaces between two phases, and the mechanics at the surface of the interface is controlled by surface tension, γ (*N/m*), which is attributed to unbalanced forces from the interaction of molecules at the surface.

When a small volume of a liquid is placed on top of a solid, the liquid forms a sessile droplet, subtending an angle at the triple line where the air, liquid, and solid interfaces meet. This equilibrium contact angle (θ) measures the wetting of the solid by the liquid. When one end of a capillary tube is brought in contact with the surface of a liquid, the liquid will form a meniscus inside the tube such that the equilibrium contact angle is satisfied and the curved interface generates a Laplace pressure at the meniscus, given by

$$\Delta P_{cap} = \frac{2\gamma \cos\theta}{R}.$$

This capillary pressure is responsible for the rise of liquids inside capillary tubes as long as the radius of the tube R is small enough such that the P_{cap} is higher than the atmospheric pressure. The $\cos\theta$ term describes tube wettability; if this term is positive (i.e., $\theta < 90$), the liquid will climb up the tube. This phenomenon is commonly known as capillary rise. A low value of contact angle can be obtained by having a low-energy liquid or a very-high-energy solid (tube surface).

surface modification of the first layer, such as plasma treatment, may be necessary. If the substrate itself is a polymer, a nanoparticle film can be prepared directly on the substrate. Nanoparticle films present high–surface area assemblies with interconnected nanopores. For example, a film of spherical SiO_2 nanoparticles made via spin coating a corresponding aqueous suspension has a porosity of ~0.35 regardless of particle size, close to that expected for a random close-packed structure. The average pore radius (R_{pore}) of random packings of spherical particles is reported to be ~30% of the particle radius (R_{NP}), although a distribution of pore sizes in such structures is inevitable (44).

This bilayer of polymer film and high–surface area nanoparticle packing is heated above the T_g of the polymer to induce CaRI. Many polymers have low surface energy and thus have wetting contact angles (i.e., <90°) on the nanoparticle surface, allowing them to rise up into the nanoparticle packing via the action of capillary forces. The capillary force pulls the polymer chains into the pores of the nanoparticle packing; this process continues until the interstitial voids in the packing are completely saturated with the polymer. The same principle has been used to induce infiltration of polymers into cylindrical pores of anodized aluminum oxide membranes (45–48). **Figure 1*a*,*b*** shows a schematic illustration and scanning electron microscopy of this process, illustrating the changes in a bilayer made of 25-nm titania (TiO_2) nanoparticle packing over polystyrene (PS; molecular weight = 8,000 g/mol) upon heating. Notably, polymer infiltration does not change nanoparticle-layer thickness. Moreover, the center-to-center distance of nanoparticles upon the completion of CaRI does not change. These results indicate that the original volume fraction of nanoparticles in the packing is retained after polymer infiltration, yielding PINFs with a high volume fraction (~65% of total volume) of nanoparticles.

The CaRI method has been used to make PINFs with nanoparticles of various chemical natures, sizes, and shapes. Polymers can easily and relatively rapidly infiltrate nanoparticle films that are several micrometers thick. Capillary energies are so dominant in this system that gravitational potentials likely play negligible roles. A simple balance between gravitational force and capillary force estimates that nanoparticle films as thick as $\sim 10^4$ m can be infiltrated via CaRI; the timescale to produce nanocomposite films that are between hundreds of nanometers

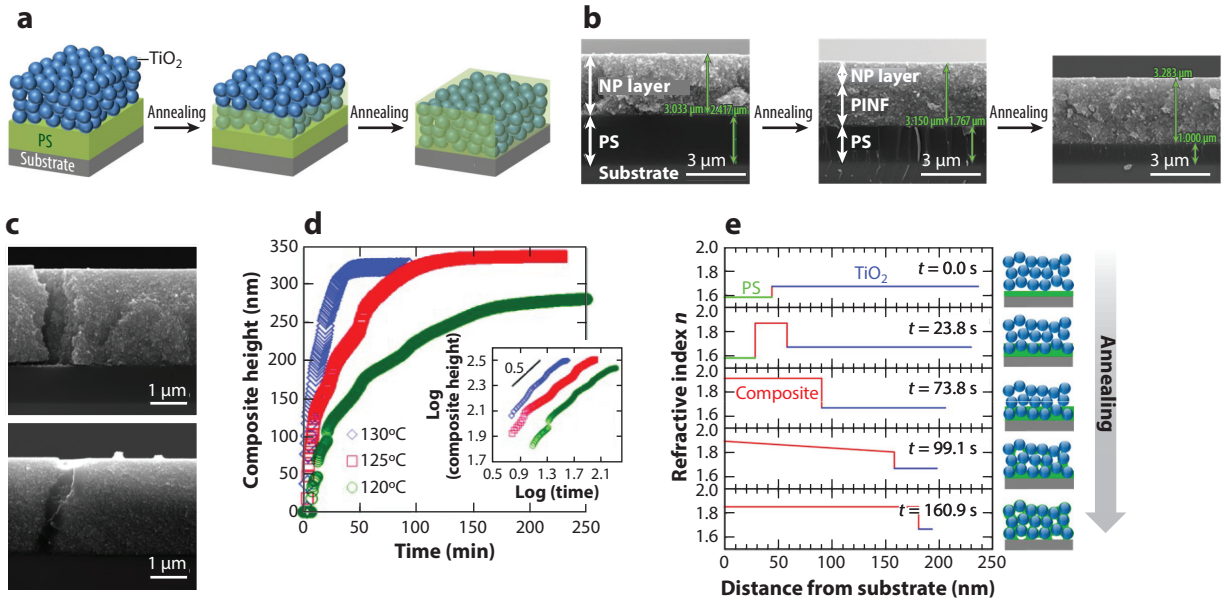

Figure 1

(*a*) Schematic illustration of capillary rise infiltration of polymer melt into a NP packing. (*b*) SEM images showing changes in polymer thickness upon infiltration and pores of NP packing filled with the polymer. (*c*) Cracks in a NP film before and after CaRI; infiltrated polymer fills the crack upon CaRI. (*d*) Composite thickness (or front height) as a function of time at three different temperatures; inset shows scaling obeys the Lucas–Washburn equation. (*e*) Refractive index profiles with bilayer heights at different stages of annealing in the UCaRI process. The schematic on the right visualizes the same. Abbreviations: CaRI, capillary rise infiltration; NP, nanoparticle; PINF, polymer-infiltrated nanoparticle film; PS, polystyrene; SEM, scanning electron microscopy; UCaRI, undersaturated capillary rise infiltration. Figure adapted with permission from References 38 and 39.

and tens of micrometers thick can range from seconds to a few hours, depending on the pore size and the molecular weight of the polymer. One advantage of CaRI is that structural defects, such as cracks and pinholes in nanoparticle films, are also filled with polymer via capillarity, offering a healing process, as shown in **Figure 1***c*.

The dynamics of polymer infiltration during CaRI can be monitored via spectroscopic ellipsometry. The PINF thickness and its optical properties, such as refractive index, can be modeled by treating an optically transparent layer using the Cauchy model (49, 50). Ellipsometric modeling of a polymer–nanoparticle bilayer undergoing CaRI shows that as the polymer rises up, it maintains a sharp front through the pores of the nanoparticle packing in the resolution of the technique. The data at any point during infiltration (except at very early times) can be modeled as a three-layer system of neat nanoparticle packing (not yet infiltrated), composite film (infiltrated nanoparticle packing), and neat polymer film (residual polymer). The growth of the composite film or the motion of the front with time provides an insight into both the dynamics of the CaRI process and ultimately the transport of the polymer chains through the pore network in the nanoparticle packing (38, 39, 51, 52).

Analysis of PS infiltrating a disordered packing of 30-nm-diameter TiO_2 nanoparticles shows that the front motion with time can be modeled using the Lucas–Washburn equation, which relates the height of the rising front (h) as a function of time (t) as (53–55)

$$h^2 = \frac{\gamma \cos\theta R_{\text{pore}}}{4\eta\tau^2} t, \qquad 1.$$

where γ is the surface tension of the polymer, θ is the equilibrium wetting angle of polymer on the nanoparticle surface, η is polymer viscosity, and h is the height of capillary rise; the term τ (~1–3) accounts for the tortuosity of the pores, and R_{pore} is the average pore radius. The scaling relationship between height and time is consistent with the Lucas–Washburn scaling at all annealing temperatures, as shown for three temperatures in **Figure 1*d***.

The case in which the volume of the polymer in the original bilayer is insufficient to completely fill the interstitial voids of the nanoparticle packing is particularly intriguing. This process, called undersaturated CaRI (or UCaRI), has been used to fabricate PINFs with homogeneous or spatially varying (graded) porosity (39). The structural evolution that takes place during UCaRI can be illustrated via an example of a PS–TiO_2 nanoparticle bilayer. Ellipsometric tracking shows that two distinct processes occur, as shown in **Figure 1*e***. In the first process, the bottom part of the nanoparticle packing is completely filled by the polymer through CaRI, which proceeds until the polymer film is completely depleted. Subsequently, polymer in the interstitial voids then enters the pores of the unfilled nanoparticle packing by surface diffusion, and a gradient in the polymer volume fraction (and hence porosity) through the thickness is developed. It is thus possible to produce PINFs with graded porosity simply by lowering the temperature below the T_g of the polymer, such that the surface diffusion of polymer is stopped before all the polymer is uniformly spread out. It is also possible to produce PINFs with uniform porosity throughout the structure by annealing the sample until the polymer evenly distributes itself throughout the nanoparticle packing. By varying the initial thickness of the polymer layer and the time of heat treatment, UCaRI PINFs of uniform or graded porosity with tunable refractive indices can be produced, which may have important implications in the fabrication of antireflection coatings or porous membranes for separation applications.

2.2. Polymers under Extreme Nanoconfinement

The remarkably versatile CaRI technique also provides a powerful platform to study polymers under extreme confinement, in which polymers display unexpected physical behaviors, relatively unexplored in the fundamental literature (47, 56–72). In CaRI composites, the average pore size in the packing of nanospheres depends on the particle radius (for spherical particles, $R_{pore} \approx R_{NP} \times 0.3$); for example, for a particle diameter of 30 nm, the average R_{pore} is 4.5 nm. The size of polymer chains, defined by the radius of gyration (R_g) of polymer, depends on the molecular weight and varies from a few nanometers to several tens of nanometers. Thus, the average chain size in CaRI can be significantly larger than the pore size; the polymer conformations will be perturbed compared with the bulk, and their behavior under strong confinement can therefore be probed via CaRI. The extent of confinement can be represented numerically by the confinement ratio (CR):

$$\mathrm{CR} = R_g/R_{pore}. \qquad 2.$$

CaRI studies using PS and silica nanoparticles have varied CRs from 0.2 to 15 by varying the size of the silica nanoparticle and the molecular weight of PS.

The significant confinement inherent in CaRI raises an important question: What is the limit to CaRI—can the CaRI process be prevented for extremely large CRs (i.e., for very large polymer chains compared with the pore or very small pores compared with the chain)? The dynamics and thermodynamics of polymer chains are dominated by their conformational entropy. When a polymer chain is physically confined, there is a significant loss in this conformational entropy because of the restrictions placed on the ability of the chain to access the entire conformational space. Moreover, physical confinement could constrict segmental motion of polymer. Thus, CaRI could be significantly impeded when CR is very large.

To understand how polymers can infiltrate despite the large CR and presumed loss of configurational entropy, the mechanism was examined theoretically and computationally by estimating the critical contact angle above which CaRI would cease to occur for a polymer infiltrating a cylindrical pore of radius R_{cyl}. The cylindrical pore, unlike the pores in a nanoparticle packing, provides a well-defined geometry to quantitatively test the hypothesis. For a simple fluid such as water, the critical contact angle would be 90°. The critical contact angle for polymers could potentially become less than 90° and could decrease further as CR increases owing to the entropic penalty. During CaRI, the loss of entropy experienced by polymer chains is counteracted by the enthalpic gain of wetting; that is, high-energy surfaces are wetted by low-energy polymers. For polymer undergoing capillary rise into a cylindrical pore, the free energy change (dF) for incremental change in the height (dh) can be expressed as

$$dF = -2\pi R_{cyl}\gamma \cos\theta dh + k_B T \rho \pi {R_{cyl}}^2 \left(\frac{Nb^2}{{R_{cyl}}^2}\right) dh, \quad 3.$$

where the first term represents the gain in enthalpy coming from pore wetting and the second term represents the loss in conformational entropy. In this expression, N and b represent the number and size of the Kuhn segments of the polymer, and ρ is the chain density. Setting $dF/dh = 0$, the critical contact angle θ_c can be expressed as

$$\cos\theta_c = \frac{\rho k_B T N b^2}{2\gamma R_{cyl}}. \quad 4.$$

Assuming that the segment density in the pore does not depend on the chain length, the chain density can be converted to segment density (ρ_0) using the number of segments per chain (N): $\rho_0 = N\rho$, which leads to

$$\cos\theta_c = \frac{\rho_o k_B T b^2}{2\gamma R_{cyl}}. \quad 5.$$

This relationship reveals that the critical contact angle depends not on the length of the chain but rather on the Kuhn segment length, which represents chain stiffness. This seemingly counterintuitive result can be rationalized by considering the fact that whereas entropy loss does depend on the molecular weight of the polymer chain, the number of polymer chains that is needed to fill a pore of a given volume is inversely proportional to the chain length.

The independence of critical contact angle on chain length and its dependence on the chain stiffness has also been verified by molecular dynamics (MD) simulations of polymers infiltrating cylindrical pores of different radii, as shown in **Figure 2*a*** (73). **Figure 2*b*** shows the variation in θ_c with chain size obtained for two polymers of different flexibility. The blue circles and triangles depict the θ_c for flexible chains, whereas the orange symbols are for semiflexible chains with some degree of stiffness incorporated into the backbone of the polymer chain. The points for both polymers lie close to the predictions from Equation 4 and show that the stiffer polymer has a lower critical contact angle.

CaRI dynamics are also altered by extreme nanoconfinement, as confirmed by in situ ellipsometry with a range of nanoparticle sizes and polymer molecular weights at different temperatures. The effect of physical confinement on the rate of infiltration of unentangled PS into packings of silica nanoparticles has been studied by varying both polymer molecular weights and particle sizes such that CR varies from 0.2 to 15 (51). To quantify the impact of confinement, the effective viscosity of polymer infiltrating a nanoparticle packing is inferred by calculating the slope from h^2 versus t data obtained from ellipsometry. Using published data for surface tension, contact angle, and pore size, the effective viscosity is estimated for each polymer–nanoparticle pair. For unentangled PS confined in silica packings, as shown in **Figure 2*d***, the confined viscosity is higher than

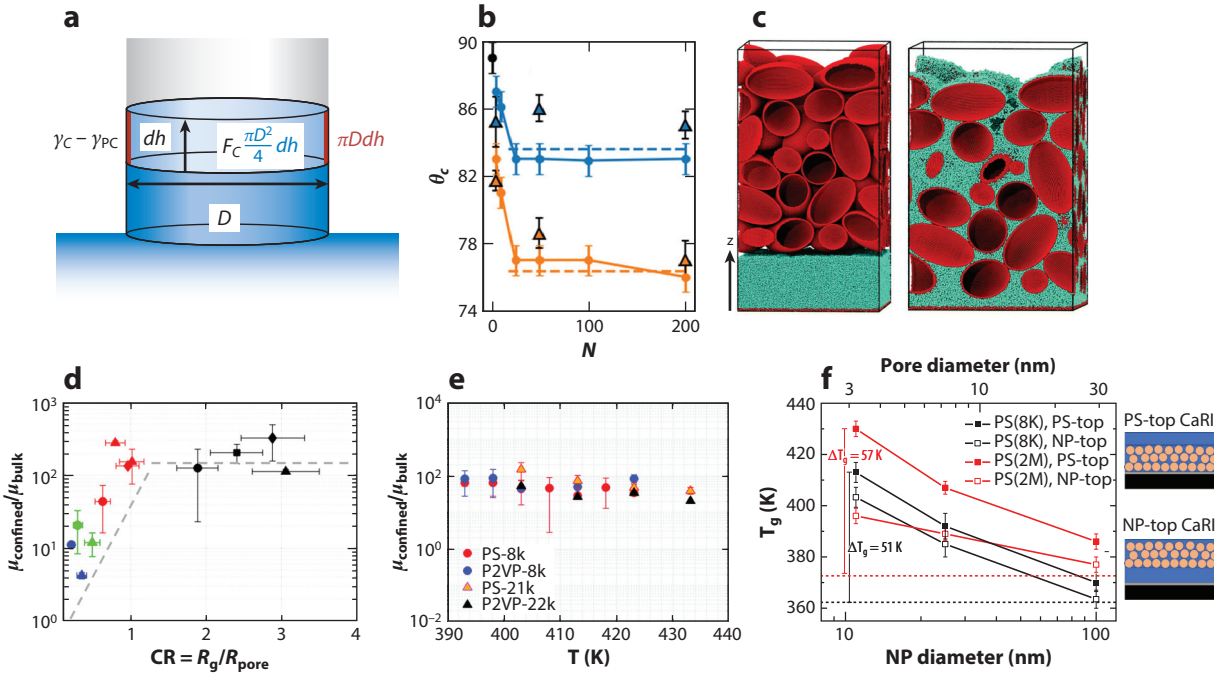

Figure 2

(*a*) A schematic detailing free energy contributions of wetting and confinement during capillary rise in a cylindrical pore. (*b*) Critical contact angle variation with number of chain segments for flexible (*blue*) and semiflexible (*orange*) polymers. (*c*) MD simulations show polymers being infiltrated into model packing of elliptical nanoparticles. (*d–f*) Normalized viscosity and change in T_g at different confinement ratios for CaRI of polymers into silica nanoparticle packings. Abbreviations: CaRI, capillary rise infiltration; CR, confinement ratio; MD, molecular dynamics; NP, nanoparticle; P2VP, poly(2-vinylpiridine); PS, polystyrene; T_g, glass transition temperature. Figure adapted with permission from References 51, 52, 73, 78, and 108.

the bulk viscosity, and the normalized value increases with increasing CR up to CR ≈ 1, beyond which the normalized viscosity plateaus at $O(\sim 10^2)$ (52).

Recently a new interpretation of the observed trends was provided based on an entropic barrier model that explains the slowdown in chain dynamics as a consequence of the entropic barriers that exist in the constricted regions of chain trajectory in the narrow pores of the NP packing (74). The model was originally developed for motion of polymer chains in concentrated polymer solutions and networks (75). The loss of conformational entropy that occurs when a chain has to move through narrow pores to navigate such highly tortuous, disordered environments forms the framework of this model. However, in the CaRI system, the loss in conformational entropy cannot be considered as the only factor contributing to polymer dynamics, since the highly favorable wetting of the polymers on the nanoparticle surface offsets the entropic penalty by the gain in wetting energy, as demonstrated in Equations 3–5.

The effect of polymer–nanoparticle interactions on the dynamics of CaRI has also been investigated using poly(2-vinylpiridine) and PS. Poly(2-vinylpiridine) is known to undergo hydrogen bonding with silica. Polymer infiltration was similar for the two systems and became slower as compared with the bulk dynamics with increasing confinement (increasing CR values), signaling a temperature-independent increase in viscosity (**Figure 2*e***). This suggests that confinement effects are more significant than the effects of polymer–nanoparticle interactions on the dynamics of

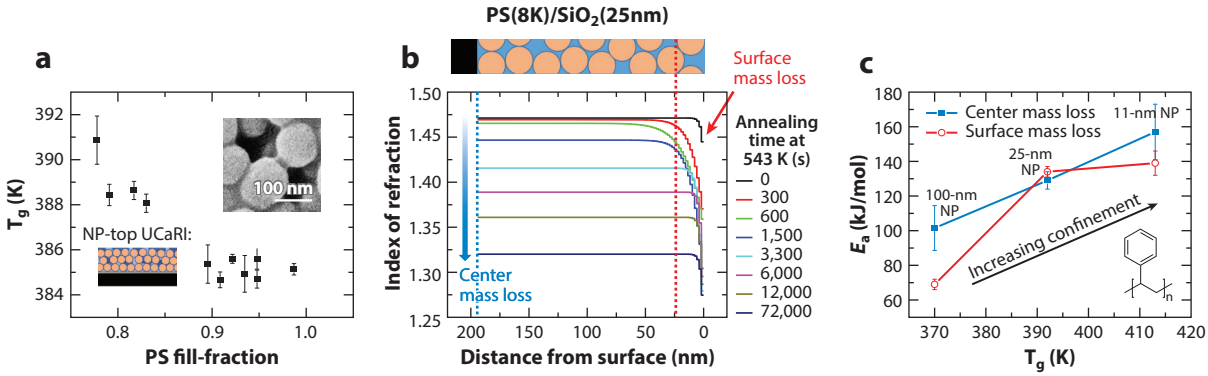

Figure 3

(*a*) T_g of PS in UCaRI films. (*b*) Two-step thermal degradation of PS in CaRI films. (*c*) Activation energy of the two steps of thermal degradation in CaRI films versus the corresponding T_g. Abbreviations: CaRI, capillary rise infiltration; NP, nanoparticle; PS, polystyrene; T_g, glass transition temperature; UCaRI, undersaturated capillary rise infiltration. Figure adapted with permission from References 78 and 82.

CaRI for unentangled polymers. This finding is similar to other nanocomposite studies, in which the extent of confinement emerges as a key parameter that slows polymer motion irrespective of the nature of interactions (76, 77).

The segmental dynamics of the polymers under confinement in CaRI composites have been probed (39, 51, 52, 78). Polymer segmental relaxation in CaRI films is significantly different than in bulk and other composite materials (78). With decreasing nanoparticle size (increasing degree of nanoconfinement), significantly slowed segmental relaxation dynamics and dramatically increased T_g were observed for PS in SiO_2 nanoparticle packings. For PS/SiO_2 CaRI films, T_g of PS can be as much as ~57 K higher than bulk (**Figure 2*f***). In UCaRI films, in which the polymer molecules gather at the particle–particle contacts with a stronger degree of confinement, the T_g can further increase by an additional 8–10 K, as shown in **Figure 3*a***. This strong decrease in T_g occurs even in the presence of a free surface that has shown enhancements in the segmental dynamics in other systems, such as ultrathin polymer films (62, 71, 79–81). Such high T_g has not been observed in similar weakly interacting systems, which indicates the strong effect of extreme nanoconfinement on the segmental relaxation of polymers.

In addition to the dramatic increase in T_g, the slowed relaxation dynamics of polymers in CaRI films can change the rate and path of the thermal degradation of polymers (82). The thermal degradation process of polymers in ambient condition is typically controlled by the diffusion of O_2, which can form highly reactive radicals with broken polymer chains. Because of limited O_2 availability, the thermal degradation of polymers is usually surface mediated and incomplete, leaving chars as the carbonization product. In PS/SiO_2 CaRI films, a two-step thermal degradation was observed: a layer-by-layer degradation on the surface region (surface mass loss) followed by uniform degradation everywhere else throughout the film (center mass loss), as shown in **Figure 3*b***. The thickness of the surface region is approximately the diameter of the nanoparticle, and the degradation rate of the center mass is independent of the total film thickness. The isothermal degradation rate of PS was found to be significantly slower under stronger nanoconfinement, and the activation energy was found to be as much as 50 kJ/mol higher than bulk (**Figure 3*c***). CaRI films are thus potential heat-resistant materials with exceptional thermal stability.

2.3. Leaching-Enabled CaRI: Using Elastomer for Patterning PINFs

An extension to CaRI relies on inducing infiltration from a polymer-/oligomer-loaded gel rather than from a pure polymer layer, enabling PINF fabrication using low-T_g polymer, and offers unique advantages, such as patterning of PINFs. Leaching-enabled CaRI (LeCaRI) takes advantage of polymer gels, like poly(dimethylsiloxane) (PDMS) elastomers, that are prepared by crosslinking of precursor chains. Several reports have shown that even when the network-formation reaction is complete, several uncrosslinked chains remain in the gel. These mobile, uncrosslinked chains have been identified as a source of contaminants, leaching out onto the air–water interface when PDMS is partially submerged in water. These uncrosslinked chains are also responsible for hydrophobic recovery when the surface of PDMS is oxidized to make it hydrophilic (83–88). When a piece of cured PDMS elastomer is brought in contact with a nanoparticle film (schematic in **Figure 4*a***), infiltration of uncrosslinked polymer into the interstices of the packing occurs, as confirmed by ellipsometry (refractive index of packing increases) and scanning electron microscopy (40). The amount of infiltration increases with contact time; 200–250-nm-thick silica packings are completely filled within 10–15 s. Soxhlet extraction of the uncrosslinked chains from the PDMS gel leads to no infiltration, verifying that the uncrosslinked chains are the main infiltrating species.

The amount of polymer infiltrated into a nanoparticle film via LeCaRI is controlled by two major factors: the amount of capillary-condensed water in the packing and the strength of capillary

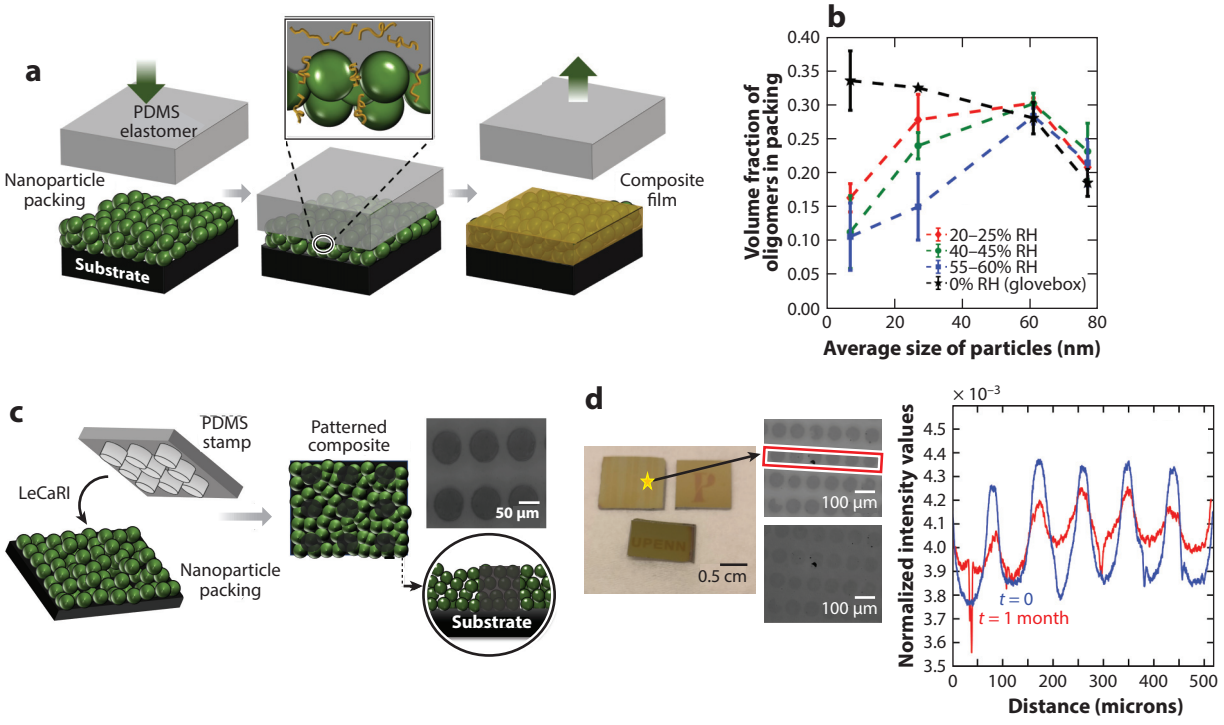

Figure 4

(*a*) Schematic illustration of LeCaRI. (*b*) The amount of infiltrated polymers with varying humidity and particle size. (*c*) Schematic of patterning using LeCaRI. (*d*) Patterns made using LeCaRI and the decrease in intensity, as measured by reflection microscope. Abbreviations: LeCaRI, leaching-enabled capillary rise infiltration; PDMS, poly(dimethylsiloxane); RH, relative humidity. Figure adapted with permission from Reference 40.

force pulling the polymer into the packing. Water condensation in the packing is controlled by the pore size and the external humidity, as described by the Kelvin equation,

$$P_{cap} = (P_{sat})e^{-\frac{\gamma \kappa V_m}{RT}}, \quad 6.$$

where P_{cap} is the pressure inside the capillary bridge (accounting for the Laplace pressure jump); P_{sat} is the saturation vapor pressure; γ and V_m are the surface tension and molar volume of the liquid, respectively; and κ is the mean curvature of the bridge in the pore. This curvature scales as $\kappa \sim -2/R_{pore}$. The smaller the nanoparticle, the higher the negative curvature of the pores, which leads to more condensation under the same ambient pressure conditions as compared with the larger nanoparticles. Thus, water condensation is favored in smaller pores, like those that form in packings of smaller nanoparticles.

The capillary force that induces LeCaRI also depends on the void size following Laplace's equation. Thus, as the particle size becomes smaller (and hence displays smaller voids), the capillary force that induces LeCaRI increases, but the water condensation that opposes LeCaRI also increases (89). In short, a trade-off exists between the amount of capillary-condensed water and the capillary pressure that induces LeCaRI; thus, maximum infiltration is realized at intermediate nanoparticle sizes. With increasing humidity, as shown in **Figure 4*b***, the amount of infiltration decreases, as indicated by a downward shift from the ambient humidity (*red*) curve for all the nanoparticle sizes. At 0% humidity in a glovebox, the amount of infiltration is the highest for the smallest nanoparticles, verifying that in the absence of capillary-condensed water, the packing that presents the strongest capillary pressure induces the largest extent of polymer infiltration via LeCaRI.

LeCaRI offers an important and potentially useful advantage of fabricating patterned PINFs. PDMS elastomers have long been used as stamps to enable microcontact printing. By preparing PDMS slabs with raised features on the surface and bringing these gels in contact with nanoparticle films, uncrosslinked chains in PDMS can be selectively infused into the regions of contact, enabling patterning of PINFs, as shown in **Figure 4*c***. These patterns fade away over time owing to the motion of chains from the patterned domains into the unpatterned regions, and the diffuse front can be tracked using reflection microscopy, as shown in **Figure 4*d***. These spreading patterns can be used to generate composites with lateral gradation. The patterns can also be permanently frozen in space by crosslinking UV-crosslinkable oligomers, which were mixed into the precursor PDMS and subsequently transferred to the nanoparticle packing via LeCaRI. Importantly, this demonstration shows that PDMS and other types of networks could potentially be used as depots to enable LeCaRI of a wide range of polymers.

LeCaRI is unique in its ability to harness the motion of polymer chains from gels into confinements in packings. This leads to opportunities in the study of motion of polymer chains from soft confinement inside gel pores into the hard confinement of the nanoparticle packing. Moreover, it will be important to understand the dynamics and thermodynamics of loading gels with a wide range of polymers and to study how the structure and compatibility of the gels and the loaded polymers affect LeCaRI.

2.4. Heterostructured PINFs via CaRI with Polymer Particles and Inorganic Nanoparticles

For many applications, heterostructured nanocomposites can provide advantages in controlling the transport, optical, and mechanical properties of coatings and membranes. For example, many separation membranes have asymmetric structures with highly selective layers atop highly porous layers that provide structural support. Multilayered films with varying refractive indices can provide structural colors or antireflection properties.

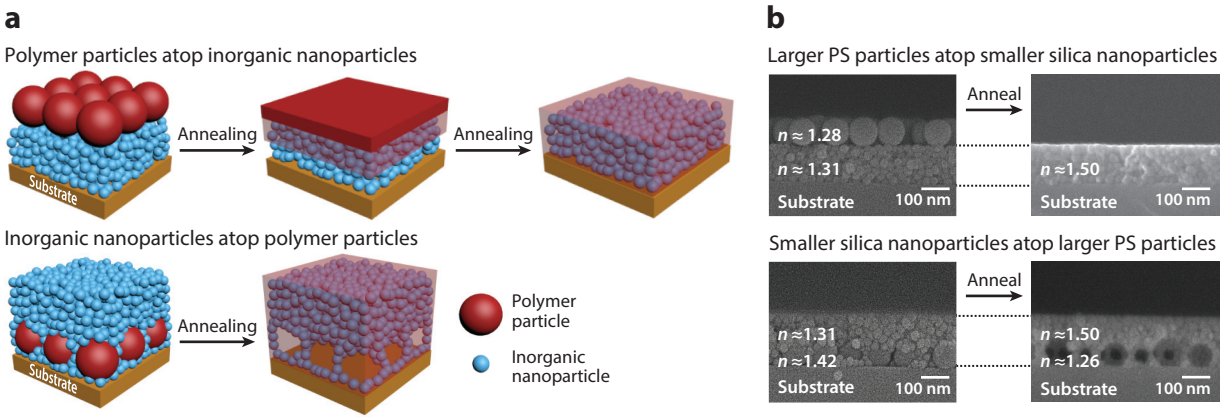

Figure 5

(*a*) Schematic illustration showing fabrication of uniform and heterostructured PINFs. (*b*) Cross-sectional SEM images of the bilayers, composed of the silica nanoparticle (25-nm) layer and PS (100-nm) particle layer, before and after annealing at 180°C for 3 h. *n* refers to refractive index. Abbreviations: PINF, polymer-infiltrated nanoparticle film; PS, polystyrene; SEM, scanning electron microscopy. Figure adapted with permission from Reference 90.

Use of polymer particles in place of a solid polymer layer in CaRI enables the fabrication of heterostructured PINFs (90). **Figure 5*a*,*b*** provides schematic illustrations showing the formation of heterostructured or uniform PINFs using polymer particles as the polymer source. In this example, the bilayer for CaRI is composed of 30-nm silica nanoparticles and 100-nm PS particles. Spin coating can be used to produce bilayers with either particle on top of the other. Interestingly, blade coating can produce bilayers with polymer particles on the bottom and smaller silica nanoparticles on top in one step, making this a potentially scalable method of producing bilayers continuously. When the nanoparticles deposited as the upper layer are sufficiently small, they can slide into the voids of the lower layer. The bilayers are then thermally annealed at a temperature above the T_g of the polymer particles to induce infiltration of polymers into the nanopores of the nanoparticle layers. For the bilayer with distinctly divided layers, the polymer layer disappears as the fluidized polymers infiltrate into the nanopores, and eventually, a PINF with a homogeneous structure is achieved, similar to the PINF resulting from the typical CaRI technique. In contrast, in the case of the bilayer in which the lower polymer particle layer is infiltrated with some of the silica nanoparticles constituting the upper layer, a PINF with a heterogeneous structure is achieved, because the infiltrated nanoparticles behave as supporting frames that prevent the collapse of the polymer layer upon CaRI. After infiltration, cavities are created where the polymer particles were originally located. The formation of these cavities significantly decreases the refractive index of the bottom layer, which has been used to produce Bragg reflector sensors, as described later in Section 5. This method of producing homogeneous or heterostructured PINFs using polymer particles also eliminates the use of organic solvents because polymer particle layers can be produced from aqueous suspensions, making it an environmentally friendly process.

3. SOLVENT-DRIVEN INFILTRATION OF POLYMER INTO NANOPARTICLE PACKINGS

3.1. Introduction to Solvent-Driven Infiltration of Polymer

Many polymers that are important for industrial applications have high or inaccessible T_g, which can make thermally induced CaRI a challenge. To address this issue, a room-temperature bilayer

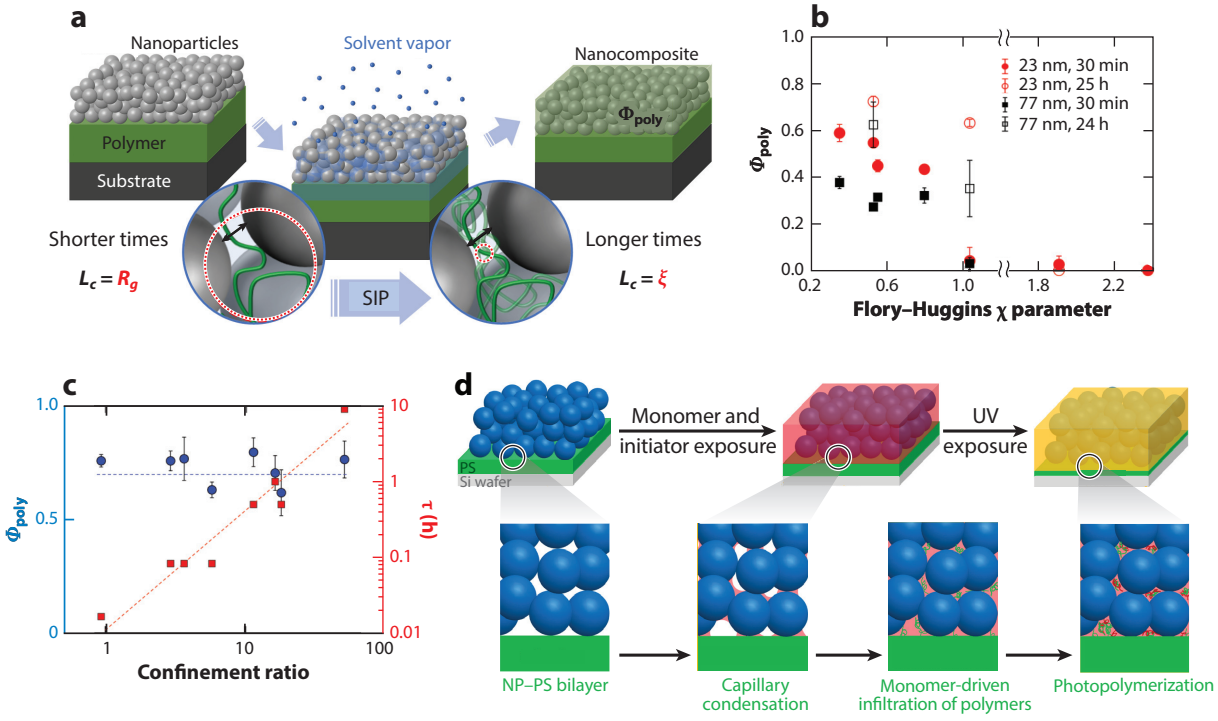

Figure 6

(*a*) Schematic illustration of SIP into a NP film; a polymer–NP bilayer is annealed with solvent vapor, leading to capillary condensation of solvent in the NP packing, followed by swelling and infiltration of polymer. The characteristic length scale (L_c) shifts from R_g to ξ as infiltration proceeds. (*b*) The volume fraction of PS in the NP packing for PS (M_n = 8,000 g/mol) into 23-nm particle packings (*circles*) and 77-nm particle packings (*squares*), after 30 min (*closed*) or 24 h (*open*) of vapor exposure for various solvents at different χ values. (*c*) Infiltration time (*red squares*, *right y-axis*) and final extent of infiltration (*blue circles*, *left y-axis*) in SIP systems as a function of confinement ratio. (*d*) Schematic illustrations of a NP–polymer bilayer being annealed with monomer and photoinitiator vapor, leading to capillary condensation of the monomer and photoinitiator, followed by infiltration of polymer, then polymerization of monomer via UV exposure. Abbreviations: NP, nanoparticle; PS, polystyrene; SIP, solvent-driven infiltration of polymer. Figure adapted with permission from References 30, 42, and 43.

infiltration technique known as solvent-driven infiltration of polymer (SIP) into nanoparticle packings has been developed (42). In SIP, a bilayer composed of a densely packed layer of nanoparticles coated on top of an underlying polymer layer is exposed to solvent vapor, which undergoes capillary condensation and floods the interstitial voids of the nanoparticle packing with liquid solvent. This solvent swells the underlying polymer layer, imparting mobility and enabling infiltration of polymer into the solvent-rich voids of the nanoparticle packing (**Figure 6*a***).

The kinetics and properties of the final composite film prepared via SIP can be tuned via solvent quality, degree of confinement, and polymer–nanoparticle interactions. Furthermore, the SIP system is robust and can be expanded to prepare PINFs with polymer blends (30) and via exposure to liquid solvent (42). This method also provides a unique opportunity to study fundamentally the infiltration of solvated polymer into highly confined solvent-filled spaces. Previous studies on the dynamics and partitioning of solvated polymer into confining spaces are limited to relatively dilute systems. Thus, they do not consider the several important aspects that occur in the SIP system (91–94). For example, in SIP, as polymer infiltrates the solvent-filled pores, the concentration shifts from dilute to highly concentrated regimes, and the polymer chains experience a high degree

of confinement. Improved understanding of these factors could provide important insights into the properties of PINFs and more generally into the physics of highly confined solvated polymers.

3.2. SIP Mechanism

The SIP process involves three phenomena: capillary condensation of solvent vapor into the interstices of the nanoparticle packing, swelling of the underlying polymer film with solvent, and infiltration of polymer into the solvent-filled voids of the nanoparticle packing. The extent of polymer infiltration in SIP is smaller than that in CaRI because the solvent occupies some volume within the pores of nanoparticle packings; subsequent evaporation of the solvent leads to the formation of nanoporous PINFs.

Capillary condensation is driven by the negative curvature of vapor–liquid interfaces that form between nanoparticles, which strongly favor condensation and lead to full flooding of these spaces if the nanoparticles are small enough, leading to very large negative curvatures at these interfaces (89). Experiments suggest that this threshold size for SiO_2 nanoparticles is smaller than 23 nm. For example, in **Figure 6*b***, polymer infiltrates a nanoparticle packing with 77-nm SiO_2 nanoparticles to a lesser degree and at a slower rate than it infiltrates a nanoparticle packing with 23-nm SiO_2 nanoparticles. This difference is attributed to incomplete capillary condensation of the larger pores in the 77-nm nanoparticle packing. For nanoparticle packings composed of particles 23 nm in diameter, complete flooding of the packing by condensed solvent is observed, allowing for faster and more complete infiltration. The final swelling extent of the underlying polymer film is found to be independent of nanoparticle size and polymer molecular weight but is dependent on solvent quality (43). Polymer infiltration into the solvent-filled nanoparticle packings in SIP depends strongly on a variety of system parameters, including solvent quality, degree of confinement, and polymer–nanoparticle interactions. In particular, solvent quality plays a major role in infiltration kinetics, with poorer solvents leading to less infiltration given the same amount of time.

One particularly interesting aspect of SIP is that confinement strongly alters SIP infiltration kinetics but does not significantly change the final infiltrated state (**Figure 6*c***). This behavior was revealed by measuring the extent of infiltration (ϕ_{poly}), defined as the volume fraction of the polymer in voids of the nanoparticle packing, and the infiltration time (τ), defined as the time required to reach the final infiltrated state, as a function of CR (Equation 2). In this study, CR was varied by changing the R_{NP} and polymer molecular weight to probe a range of CRs that cover nearly two orders of magnitude. Infiltration dynamic results presented in **Figure 6*c*** (*red squares*, *right y-axis*) reveal a strong power-law dependence for the infiltration time on the CR, with $\tau \sim CR^{3/2}$, which falls between the predicted scaling for a dilute polymer solution ($\tau \sim CR^{3/2}$) and for a melt ($\tau \sim CR^2$). This behavior is attributed to the fact that as SIP proceeds, the infiltrated polymer crosses over multiple concentration regimes. Notably, as the polymer crosses through these regimes, the characteristic length scale of the polymer shifts from R_g to the correlation length (ξ). The final infiltrated state in a good solvent, shown in **Figure 6*c*** (*blue circles*, *left y-axis*), reveals that the CR does not impact the final extent of infiltration. This is because at long times, infiltration occurs under highly concentrated conditions, where the characteristic length scale of the polymer is the molecular weight–independent correlation length (ξ), which for PS is comparable to or slightly smaller than the smallest pore size considered in the study.

The SIP system can also be used to prepare PINFs with polymer blends by using a monomer as the solvent vapor. In this variant of the technique, condensed liquid monomer and initiator are used to infiltrate an underlying polymer film via SIP, followed by exposure to UV light, which leads to polymerization of the condensed monomer within the nanoparticle packing (30) (**Figure 6*d***). The ratio of polymers in the final blend composite can be tuned by controlling the thickness of the initial underlying polymer film and the duration of exposure to UV light.

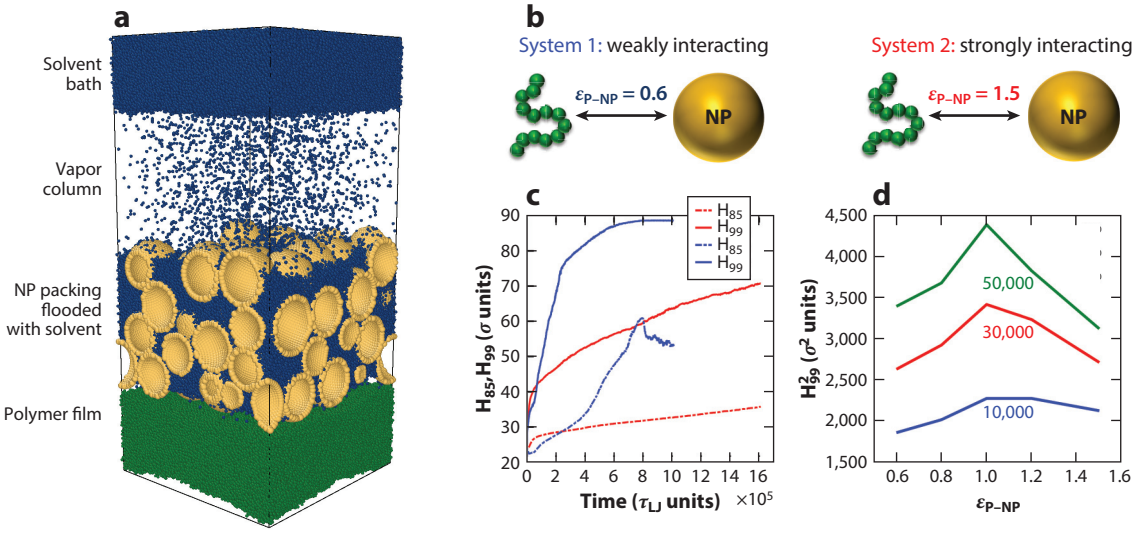

Figure 7

(*a*) A model system for solvent-driven infiltration of polymer molecular dynamics simulations. (*b*) Choice of interaction potential between polymer and NP in the model system. (*c*) Averaged front position (H_{99},H_{85}) of infiltration front with time for $\varepsilon_{P-NP} = 0.6$ (*blue*) and $\varepsilon_{P-NP} = 1.1$ (*red*). (*d*) Squared front position (H_{99}^2) versus interaction parameter (ε_{P-NP}) at three different times during infiltration for $T = 0.7$. Abbreviations: NP, nanoparticle; P, polymer. Figure adapted with permission from Reference 41.

The interplay of solvent-quality effects and polymer–nanoparticle interaction effects on the dynamics of SIP has also been explored by using MD simulations (**Figure 7*a*,*b***), which show that three regimes can emerge: solvent-mediated infiltration, when the polymer–nanoparticle interactions are very weak; surface-mediated infiltration, when there are strong polymer–nanoparticle interactions; and solvent- and surface-mediated infiltration, when the strength of polymer–nanoparticle interactions are in the intermediate range (41). These regimes are explored by changing the Lennard–Jones interaction energy (ε_{P-NP}) between polymer beads and the nanoparticle surface over a wide range while keeping the interaction energies between the polymer and solvent and the solvent and nanoparticle constant. Polymer infiltrates much faster when the polymer–nanoparticle interaction is weak ($\varepsilon_{P-NP} = 0.6$) as opposed to when there are strong interactions ($\varepsilon_{P-NP} = 1.5$). Moreover, there is a more diffuse front when the polymer–nanoparticle interactions are weak, which can be observed in the simulations as a greater difference between the fastest ninety-ninth percentile and the closer to bulk eighty-fifth percentile of infiltrating polymers. The fastest kinetics are predicted to occur in an intermediate ($\varepsilon_{P-NP} = 1$) polymer–nanoparticle interaction regime (**Figure 7*d***). This nonmonotonic dependence on polymer–nanoparticle interactions may be due to the polymer avoiding the nanoparticle surface at very low polymer–nanoparticle interaction strength, which limits the available pathways for polymer infiltration, and the advent of adsorption at high polymer–nanoparticle interaction strengths, which slows chain relaxation, leading to slower infiltration. At intermediate interaction strengths, multiple infiltration pathways are available, leading to faster infiltration kinetics.

4. MECHANICAL PROPERTIES OF CARI/SIP PINFS

4.1. Hardness and Elastic Modulus

The high loadings of nanoparticles in PINFs produced via CaRI provide the opportunity to realize materials with high stiffness and high hardness relative to polymers and many polymer

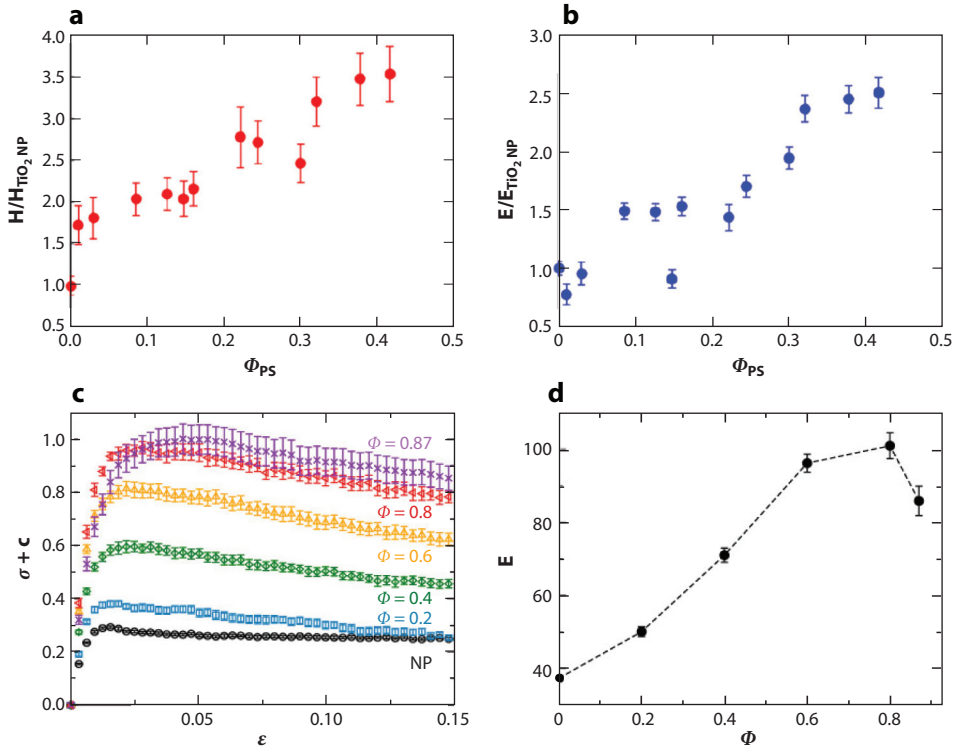

Figure 8

The normalized (*a*) hardness and (*b*) modulus of PINFs as a function of PS volume fraction (Φ_{PS}) obtained from nanoindentation measurements with a Berkovich indenter tip. The neat TiO_2 NP film's hardness and reduced modulus are 271.6 ± 21.4 MPa and 12.9 ± 0.5 GPa, respectively. (*c*) Stress-strain for a neat NP packing and PINFs with different filling fraction under uniaxial tension in molecular dynamics simulations and (*d*) elastic moduli of PINFs extracted from panel *c*. Abbreviations: NP, nanoparticle; PINF, polymer-infiltrated nanoparticle film; PS, polystyrene. Figure adapted with permission from References 39 and 99.

nanocomposites. The stiffness and hardness of UCaRI films made with PS (MW ≈ 8,000 g/mol) and TiO_2 nanoparticles (major axis $2b = 37.4 \pm 6.7$ nm, minor axis $2a = 28.8 \pm 4.1$ nm) have been measured via quasi-static nanoindentation (39). As shown in **Figure 8*a*,*b***, both the hardness and modulus of PINFs increase as a function of ϕ_{PS}. Here, ϕ_{PS} is defined as the volume fraction of PS in each film; i.e., $\phi_{PS} = h_{PS}/h_{TiO2}$, where h_{PS} and h_{TiO2} are the initial thickness (before infiltration) of the PS layer and TiO_2 nanoparticle layer, respectively. The hardness and modulus of fully infiltrated PINFs can reach 3.5 and 2.5 times those of neat TiO_2 nanoparticle films, respectively, and 4.6 and 3.3 times the pure polymer films, respectively. The modulus value is believed to be the largest that has been reported for PS–TiO_2 nanoparticle composites (95–98).

In addition to the experimental measurements, MD simulations of coarse-grained, polymer-infiltrated random-close-packed nanoparticle packings under uniaxial tension have been performed to predict mechanical properties of undersaturated PINFs (99). Standard model polymers are used in these simulations with harmonic bonds between nearest neighbors, and pairwise interactions governed by LJ potential are used to describe nonbonded interactions. MD-predicted uniaxial stress-strain curves of neat nanoparticle film and PINFs as a function of polymer fill fraction (ϕ) are shown in **Figure 8*c***. The elastic modulus (**Figure 8*d***) is extracted as the initial slope

of these curves. Here, in contrast to ϕ_{PS} defined above, ϕ is defined as the number density of polymer monomers in the void volume of the nanoparticle packing ranging from 0.2 to 0.87, i.e., $\phi = N_{poly}/(V_{box} - V_{NP})$, where N_{poly} is the total number of polymer monomers, V_{box} is the volume of the simulation box, and V_{NP} is the total volume of all of the nanoparticles. Below $\phi = 0.87$, the yield stress and elastic modulus increase with ϕ, consistent with experimental results. The decrease in elastic modulus for PINFs with $\phi = 0.87$ may be attributed to the different mode of deformation in experiments and simulations. By calculating the average fraction of polymer chains f_{bridge} that make contact with more than one nanoparticle, it was found that the majority of the polymer chains ($f_{bridge} > 0.7$) make bridges between multiple nanoparticles at the highest polymer loading, and f_{bridge} increases as ϕ decreases. This indicates that the source of hardness and modulus enhancement is the polymer bridging effect that strengthens the interactions between the nanoparticles and allows them to better accommodate strain without breaking.

4.2. Fracture Toughness

The fracture toughness, which is a measure of resistance to crack propagation, of PINFs has also been investigated. The fracture toughness of UCaRI PINFs has been characterized by a pillar-splitting method in which micropillars that are milled via focused ion beam are indented using a pyramidal tip (100) (**Figure 9*a*,*b***). The micropillar test is used, as it can readily be applied to thin films and allows for a statistically significant number of measurements to be done on a single sample (101). As shown in **Figure 9*c***, by increasing ϕ_{PS} from 0 to 0.32, the fracture toughness of PINF is enhanced by almost an order of magnitude, from 0.07 to 0.65 MPa·m$^{1/2}$.

Several toughening mechanisms contribute to the increase in toughness with increasing ϕ_{PS}. One mechanism is the formation of polymer capillary bridges [as confirmed by scanning electron microscopy (SEM) images and MD simulations] at low ϕ_{PS}, which increases the contact area and strengthens the nanoparticle contacts. For example, the fracture toughness of PINFs with $\phi_{PS} = 0.03$ (0.25 MPa·m$^{1/2}$) is approximately 3.5 times that of neat nanoparticle films (0.07 MPa·m$^{1/2}$). A second mechanism is the nanoconfinement-induced polymer bridging of nanoparticles, which is most apparent in PINFs with low ϕ_{PS} and high molecular weight (**Figure 9*d***). For PINFs with $\phi_{PS} = 0.01$ and 0.03, enhancement in fracture toughness increases with the molecular weight of the infiltrated PS. As polymer infiltrates into nanoparticle packings, chains are highly confined by the small pores and are thus forced to stretch to fit into the pores. During fracture, polymer with high molecular weight stretches over larger distances and bridges multiple nanoparticles. As a result, more energy is dissipated during crack propagation, and the fracture toughness is enhanced significantly. For $\phi_{PS} = 0.03-0.32$, the fracture toughness of PINF increases superlinearly with ϕ_{PS}. PINF toughness is also increased through crack pinning and deflection; cracks are deflected around hard nanoparticles and propagate through the soft PS or at PS–nanoparticle interfaces. These multiple toughening effects are synergistic and change the underlying mechanism of deformation. **Figure 9*a*** shows an SEM image of fractured neat nanoparticle pillars, which exhibit through-thickness cracks, indicating brittle fracture. In comparison, the fractured PINF pillars (**Figure 9*b***) conform to indenter tip geometry and undergo a more homogeneous deformation, indicating enhanced plasticity.

4.3. Scratch and Wear Resistance

Scratch and wear resistance of TiO_2/PS PINFs prepared by CaRI have been characterized via nanoindentation-based sliding tests and contact mode atomic force microscopy, respectively (38). Scratch tests are very useful for comparative and qualitative evaluation of the resistance of different coatings to mechanical surface damage that can occur during handling and usage. The infiltration

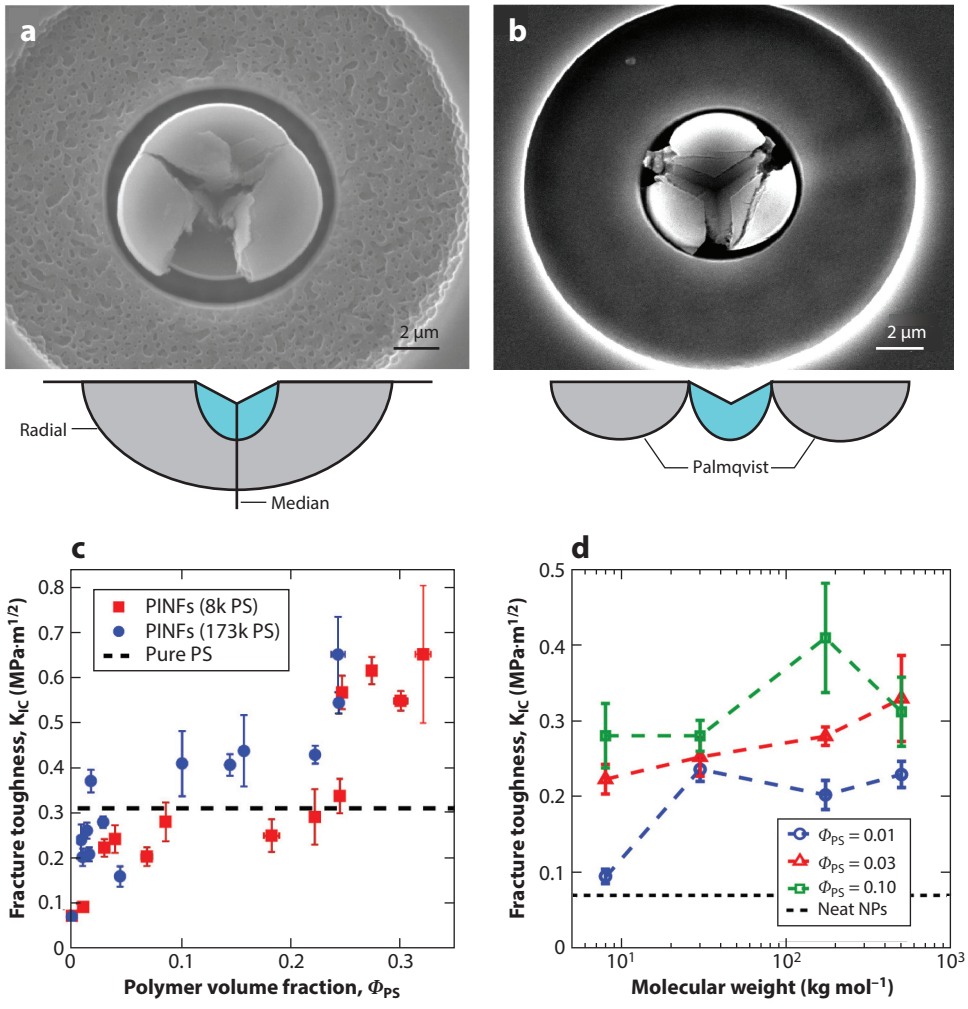

Figure 9

Scanning electron microscopy images of fractured micropillars milled from (*a*) neat NP film and (*b*) PINFs with $\Phi_{PS} = 0.27$. Schematic illustrations of corresponding crack types are also shown where cracks and plastic zones are represented by gray and blue, respectively. (*c*) Fracture toughness of PINFs filled with 8k PS and 173k PS as a function of polymer volume fraction Φ_{PS}. The dotted line indicates the mean fracture toughness value of the pure 8k and 173k PS films. (*d*) Fracture toughness of PINFs with different polymer volume fractions and molecular weight. Abbreviations: NP, nanoparticle; PINF, polymer-infiltrated nanoparticle film; PS, polystyrene. Figure adapted with permission from Reference 100.

of a polymer significantly enhances the scratch and wear resistance of nanoparticle films. For example, results of atomic force microscopy–based wear tests show that the average wear depth of a fully infiltrated PINF was 39% and 18% lower than that of a neat TiO_2 film after 1 and 5 wear scans, respectively (38), indicating that PINFs have enhanced surface durability.

In summary, infiltrating nanoparticle packings with polymers leads to concurrent increases in hardness, modulus, scratch/wear resistance, and fracture toughness. Remarkably, the mechanical reinforcement is significant even at low polymer volume fraction ($\phi \approx 0.01$) owing to the polymer bridging effect. This makes polymer infiltration a versatile method to fabricate composite coatings

with tunable porosity and mechanical properties. Our ongoing work aims to systematically study the effect of particle shape/size and polymer–nanoparticle interactions on the fracture properties of PINFs.

5. APPLICATIONS OF PINFS PREPARED VIA CARI OR SIP

An essential advantage of CaRI and SIP is that a wide range of materials can be used for PINF fabrication. These include PINFs made with nanoparticles of different types, shapes, and orientations. Moreover, various types of polymers, including both high- and low-T_g thermoplastics, resins, and semicrystalline polymers, can be used to produce multifunctional PINFs. PINFs prepared based on CaRI or SIP have enhanced and, at times, emergent properties and functionality owing to the presence of extremely high volume fractions of nanoparticles. This section highlights recent reports that take advantage of the composition, morphology, and functionality of CaRI/SIP-based PINFs in a wide range of applications (102, 103).

5.1. Suppression of Thermal Degradation and Boundary Scattering in Heat Transfer

As briefly described in Section 2.3, infiltration of PS into the interstices of silica nanoparticle films induces drastic changes in the thermal degradation properties of the polymer. As the size of silica nanoparticle decreases, the isothermal degradation time and the activation energy for thermal degradation increase, which also correlate well with the increase in T_g of PS in these PINFs. The characteristic degradation time at a fixed isothermal degradation temperature increases by as much as 30 times when the size of the silica nanoparticles is 11 nm compared with 100 nm for 8k PS. Moreover, the flammability of PS in PINFs is reduced significantly also, as evidenced by reduced char formation. Detailed ellipsometry study revealed that the degradation of confined polymer is diffusion limited and that the enhanced thermal stability is due to the slower diffusion of the free radicals, oxygen, and reaction products (82).

PS infiltration into silica nanoparticle films also induces unexpected changes in the heat transfer properties of the silica nanoparticle films (104). In disordered packing of NPs, the scattering of heat-carrying phonons occurs across each particle boundary (in the interparticle junctions and the voids of the packings), reducing the total thermal conductivity of the NP packing—a phenomenon known as boundary scattering. In a work by Donovan et al. (104), a thermal transport mechanism in disordered packings of SiO_2 nanoparticles was characterized to quantify the impact of thermal boundary scattering upon polymer infiltration at nanoparticle interfaces. The interstitial PS was found to significantly eliminate boundary scattering, leading to an increase in the overall thermal conductivity of the PINF, which cannot be predicted based on the effective medium theory and the minimum thermal conductivity limit. As **Figure 10*a*** shows, the PINF obtained via infiltration techniques has improved thermal conductivity over the silica nanoparticle film owing to elimination of boundary scattering. Conventionally, thermal conduction is considered to arise from vibration and collision of molecules as well as the propagation and collisions of phonons. It has been proposed that phonon scattering, which negatively impacts thermal conduction, can be reduced by eliminating interfaces by filling voids and particle junctions with materials that can match the vibrational properties of the nanoparticles. Stiff interstitial PS improves heat transmission through the nanoparticle interface by eliminating the boundary scattering at interfaces and restoring the system to a composite state controlled only by intrinsic scattering of phonons. These results suggest that the thermal properties in disordered nanoparticle packings, which typically exhibit low thermal conductivities owing to extremely large boundary scattering at the nanoparticle surface, can be enhanced through the vibrational thermal bridging by infiltrated polymers via CaRI or SIP.

5.2. Superhydrophobic Composite Films with Anti-Reflection and Anti-Icing Properties

Nanocomposite films consisting of vertically aligned high–aspect ratio nanowires (NWs) have several useful properties owing to their unique morphology. One of the key challenges in producing such nanocomposite films is retaining vertical alignment of high–aspect ratio NWs during

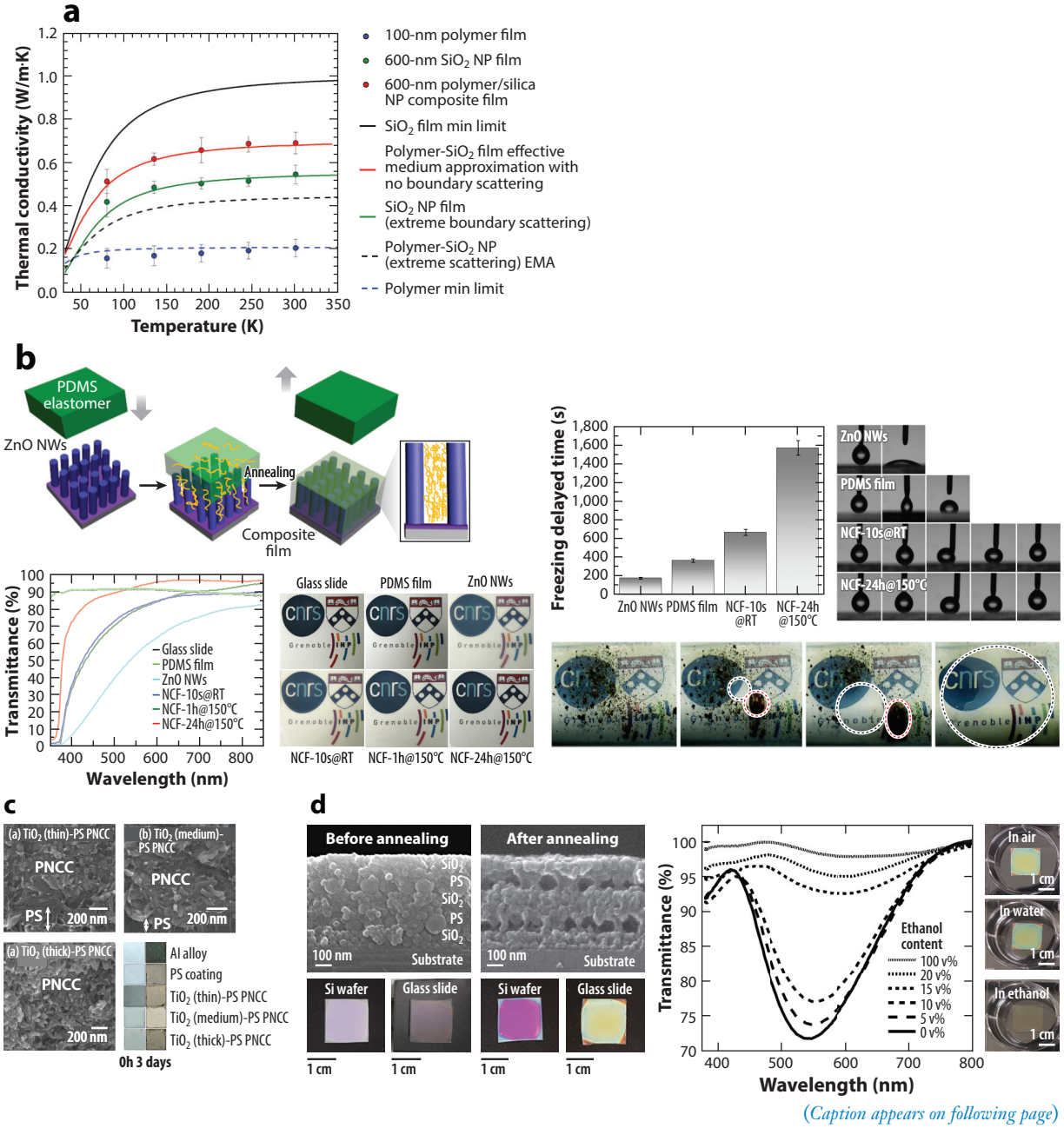

(*Caption appears on following page*)

Figure 10 (*Figure appears on preceding page*)

(*a*) Thermal conductivity of polymer-infiltrated NP films and silica NP films and thermal modeling results with boundary scattering eliminated (*red curve*) and included (*green curve*). (*b*) Clockwise from top: zinc oxide (ZnO) NWs infiltrated with PDMS oligomers; anti-icing and superhydrophobic properties of the composite materials; composite surface self-cleaning properties (shown here after subsequent rounds of washing); optical properties show composite materials are highly transparent. (*c*) Anticorrosion coatings made on Al alloy by infiltration of PS into titania NP packings. (*d*) Cross-sectional SEM images and top-down digital images of the multilayers with five alternating SiO_2 (30-nm) and PS (100-nm) NP layers, before and after annealing at 180°C for 3 h (*left*). Transmittance spectra and top-down digital images of the annealed multilayers with the seven layers in various solvents (*right*). Abbreviations: EMA, effective medium approximation; NCF, nanocomposite film; NP, nanoparticle; NW, nanowire; PDMS, poly(dimethylsiloxane); PNCC, polystyrene (PS)/TiO_2 nanocomposite coatings; PS, polystyrene; SEM, scanning electron microscopy. Figure adapted with permission from References 90, 104, 105, and 107.

nanocomposite fabrication. Nanocomposite films with vertically aligned ZnO NWs (schematic in **Figure 10*b***) were fabricated by inducing LeCaRI of uncrosslinked and mobile oligomer chains from a PDMS slab into the crevices between vertically aligned ZnO NWs (105). PDMS oligomer-infiltrated ZnO NW films demonstrated several useful properties, including superhydrophobicity and self-cleaning properties. The nanocomposite films also showed an excellent recovery in superhydrophobicity after being compromised through repeated plasma treatments or even exposure to intense UV irradiation. The infiltration of PDMS oligomers into the interstices significantly reduced the light scattering of ZnO NWs and even led to antireflection properties by reducing the difference in the refractive index between the NW phase and the continuous phase of the nanocomposite film. Moreover, PDMS oligomer-infiltrated ZnO NW nanocomposite films significantly suppressed the formation of ice nuclei and the growth rate of ice crystals compared with neat ZnO NW arrays and PDMS films at a temperature of −15°C. Significantly longer freezing times indicate that PDMS oligomer-infiltrated ZnO NW nanocomposite films could be highly desirable in applications that require deicing because water droplets can easily slide off with a slight tilting angle or with mild vibration before they undergo icing.

5.3. Water–Oil Separation

As demonstrated in the study of superhydrophobic surfaces prepared via LeCaRI of hydrophobic oligomers into an array of vertically aligned ZnO NWs, CaRI provides a versatile approach to fabricate films with extreme wetting properties. Zeng et al. (106) demonstrated a very useful application of such an approach in oil–water separation by producing PINFs made of hydrophobic silica nanoparticles and acrylic resin on stainless steel mesh (SSM). SSM was coated with acrylic resin and subsequently with a layer of hydrophobic silica nanoparticles via spray coating. The acrylic resin/SiO_2 nanoparticle bilayer–coated SSM was subsequently heated above the T_g of the resin to produce PINF-coated SSM. The PINF-coated SSM could separate an oil–water mixture for at least 50 cycles and could readily recover its separation properties after the surface was intentionally damaged via mechanical abrasion.

5.4. Anticorrosion Coatings

In addition to the excellent mechanical properties afforded by PINFs produced via CaRI, these coatings could also be used to inhibit surface corrosion. PINFs made of TiO_2 nanoellipsoids (33 nm in width and 206 nm in length) and PS (molecular weight ≈ 8,000) were fabricated via CaRI on AA2024-T3 aluminum (107). The TiO_2–PS PINF coating showed excellent corrosion suppression compared with coatings made purely of PS in a 3.5 wt% NaCl solution. Interestingly, the PINF with no residual PS layer (i.e., in which the amount of PS was just sufficient to fully fill the interstices of TiO_2 nanoparticle packing) provided the best corrosion protection.

5.5. Bragg Reflector Sensors

As highlighted earlier, CaRI with inorganic silica nanoparticles and PS nanoparticles presents a unique opportunity to fabricate heterostructured PINFs with alternating refractive indices; the layer that used to have PS nanoparticles ends up with cavities that significantly lower its refractive index, whereas the refractive index of the SiO_2 layer is significantly increased upon CaRI as voids are filled with the polymer. Such a large difference in the refractive index between the two layers can be used to produce Bragg reflectors, one-dimensional photonic crystals formed from multilayers of alternating stacks of high and low refractive indices. A Bragg reflector with a strong reflectance band in the visible region produces what is known as structural color. The intensity and spectral wavelength of the reflectance band depend on the number of alternating layers, the thickness of each stack, and the difference in the refractive indices of the two stacks.

Bragg reflectors fabricated via CaRI with SiO_2 and PS nanoparticles show strong reflectance in the visible region of the spectrum. Moreover, because the cavity is coated with PS, a hydrophobic polymer, water cannot infiltrate these cavities when an entire Bragg reflector is submerged under water. In contrast, ethanol can easily infiltrate and fill these cavities, increasing the refractive index of the cavity containing stacks and significantly reducing the reflectance. As seen in the right side of **Figure 10*d***, the strong color of the Bragg reflector is evident in air and water, whereas it disappears in ethanol. The intensity of the structural color depends on the concentration of ethanol in water, enabling colorimetric sensing of ethanol at fairly low concentrations of 15% (90). This study also demonstrated that other types of liquids or chemicals can induce the wetting transition of the cavity surface within the Bragg reflectors to enable their presence in water.

SUMMARY POINTS

1. Nanocomposite coatings and membranes with high concentrations of nanomaterials (above 50 vol%) exhibit functionality and properties that take advantage of high volume fractions of nanoparticles of different types, shapes, and alignments. This review has highlighted recent works that use capillarity-based routes such as capillary rise infiltration (CaRI) and solvent-driven infiltration of polymer (SIP) to produce such highly loaded polymer-infiltrated nanoparticle films (PINFs). CaRI and SIP provide versatile and potentially scalable methods of producing PINFs with a wide range of materials.
2. CaRI and SIP provide a unique platform to study the dynamics and thermodynamics of polymers under extreme nanoconfinement. These fundamental studies have already led to some intriguing and unexpected results that present new questions.
3. Extremely high concentrations of nanoparticles in PINFs prepared via CaRI and SIP will lead to new properties and functionality that have not been attainable in conventional nanocomposite systems. In particular, it may be possible to produce cross-functional films that overcome property trade-offs that are often observed in nanocomposite materials. Owing to their unique morphology and composition, these composites exhibit both high toughness and high strength.

FUTURE ISSUES

1. Fundamentally, the limitations of CaRI and SIP methods have not been addressed fully. These methods are extremely powerful in inducing infiltration of polymers. It is critical

to find circumstances (e.g., nanoparticle–polymer pair) and parameters that greatly or completely suppress infiltration of a polymer into a nanoparticle packing.

2. Inducing infiltration of polymers of different architecture and morphology also will lead to new understanding and potential functionality. For example, the phase behavior of semicrystalline polymers, polymer blends, and block copolymers in PINFs prepared via CaRI and SIP presents myriad intriguing possibilities and questions.
3. Other applications that are particularly suited for PINFs prepared via CaRI and SIP include gas barrier coatings and films, which are extremely important packaging materials. In particular, PINFs made with highly anisotropic nanomaterials, such as nanoplatelets, likely will drastically reduce the passage of gases and vapor owing to the high tortuosity present in these materials. CaRI and SIP methods can be extended to produce PINFs with functional nanoparticles (such as graphene and carbon nanotubes) that have unique electronic, optical, catalytic, and magnetic properties.

DISCLOSURE STATEMENT

The authors are not aware of any affiliations, memberships, funding, or financial holdings that might be perceived as affecting the objectivity of this review.

ACKNOWLEDGMENTS

This work was supported by a Penn MRSEC grant (NSF-DMR 1720530) and National Science Foundation grants 1545884, 1662695, and 1933704.

LITERATURE CITED

1. Odegard GM, Clancy TC, Gates TS. 2005. Modeling of the mechanical properties of nanoparticle/polymer composites. *Polymer* 46(2):553–62
2. Sen S, Thomin JD, Kumar SK, Keblinski P. 2007. Molecular underpinnings of the mechanical reinforcement in polymer nanocomposites. *Macromolecules* 40(11):4059–67
3. Bockstaller MR, Thomas EL. 2003. Optical properties of polymer-based photonic nanocomposite materials. *J. Phys. Chem. B* 107(37):10017–24
4. Flory F. 2011. Optical properties of nanostructured materials: a review. *J. Nanophotonics* 5(1):052502
5. Chandra A, Turng L-S, Gopalan P, Rowell RM, Gong S. 2008. Study of utilizing thin polymer surface coating on the nanoparticles for melt compounding of polycarbonate/alumina nanocomposites and their optical properties. *Compos. Sci. Technol.* 68(3–4):768–76
6. Winey KI, Kashiwagi T, Mu M. 2007. Improving electrical conductivity and thermal properties of polymers by the addition of carbon nanotubes as fillers. *MRS Bull.* 32(4):348–53
7. Qin S, Pour MG, Lazar S, Köklükaya O, Gerringer J, et al. 2019. Super gas barrier and fire resistance of nanoplatelet/nanofibril multilayer thin films. *Adv. Mater. Interfaces* 6(2):1801424
8. Holder KM, Cain AA, Plummer MG, Stevens BE, Odenborg PK, et al. 2016. Carbon nanotube multilayer nanocoatings prevent flame spread on flexible polyurethane foam. *Macromol. Mater. Eng.* 301(6):665–73
9. Liu X, Qin S, Li H, Sun J, Gu X, et al. 2019. Combination intumescent and kaolin-filled multilayer nanocoatings that reduce polyurethane flammability. *Macromol. Mater. Eng.* 304(2):1800531
10. Holder KM, Smith RJ, Grunlan JC. 2017. A review of flame retardant nanocoatings prepared using layer-by-layer assembly of polyelectrolytes. *J. Mater. Sci.* 52(22):12923–59

11. Farrokhnia M, Safekordi A, Rashidzadeh M, Khanbabaei G, Akbari Anari R, Rahimpour M. 2016. Development of porous nanocomposite membranes for gas separation by identifying the effective fabrication parameters with Plackett-Burman experimental design. *J. Porous Mater.* 23(5):1279–95
12. Jeong B-H, Hoek EMV, Yan Y, Subramani A, Huang X, et al. 2007. Interfacial polymerization of thin film nanocomposites: a new concept for reverse osmosis membranes. *J. Membr. Sci.* 294(1–2):1–7
13. Müller K, Bugnicourt E, Latorre M, Jorda M, Echegoyen Sanz Y, et al. 2017. Review on the processing and properties of polymer nanocomposites and nanocoatings and their applications in the packaging, automotive and solar energy fields. *Nanomaterials* 7(4):74
14. Harito C, Bavykin DV, Yuliarto B, Dipojono HK, Walsh FC. 2019. Polymer nanocomposites having a high filler content: synthesis, structures, properties, and applications. *Nanoscale* 11(11):4653–82
15. Parveen N, Ansari MO, Cho MH. 2016. Route to high surface area, mesoporosity of polyanilinetitanium dioxide nanocomposites via one pot synthesis for energy storage applications. *Ind. Eng. Chem. Res.* 55(1):116–24
16. Lu L, Luo Z, Xu T, Yu L. 2013. Cooperative plasmonic effect of Ag and Au nanoparticles on enhancing performance of polymer solar cells. *Nano Lett.* 13(1):59–64
17. Wu J-L, Chen F-C, Hsiao Y-S, Chien F-C, Chen P, et al. 2011. Surface plasmonic effects of metallic nanoparticles on the performance of polymer bulk heterojunction solar cells. *ACS Nano* 5(2):959–67
18. Rajesh, Ahuja T, Kumar D. 2009. Recent progress in the development of nano-structured conducting polymers/nanocomposites for sensor applications. *Sens. Actuators B* 136(1):275–86
19. Tjong SC. 2012. Polymer nanocomposites for sensor applications. In *Polymer Composites with Carbonaceous Nanofillers*, pp. 351–79. Weinheim, Ger.: Wiley-VCH Verlag GmbH & Co. KGaA
20. Bonnet P, Sireude D, Garnier B, Chauvet O. 2007. Thermal properties and percolation in carbon nanotube-polymer composites. *Appl. Phys. Lett.* 91(20):201910
21. Song DP, Li C, Li W, Watkins JJ. 2016. Block copolymer nanocomposites with high refractive index contrast for one-step photonics. *ACS Nano* 10(1):1216–23
22. Munch E, Launey ME, Alsem DH, Saiz E, Tomsia AP, Ritchie RO. 2008. Tough, bio-inspired hybrid materials. *Science* 322(5907):1516–20
23. Bonderer LJ, Studart AR, Gauckler LJ. 2008. Bioinspired design and assembly of platelet reinforced polymer films. *Science* 319(5866):1069–73
24. Sellinger A, Weiss PM, Nguyen A, Lu Y, Assink RA, et al. 1998. Continuous self-assembly of organic-inorganic nanocomposite coatings that mimic nacre. *Nature* 394(6690):256–60
25. Chen Q, Gong S, Moll J, Zhao D, Kumar SK, Colby RH. 2015. Mechanical reinforcement of polymer nanocomposites from percolation of a nanoparticle network. *ACS Macro Lett.* 4(4):398–402
26. de Jongh PE, Eggenhuisen TM. 2013. Melt infiltration: an emerging technique for the preparation of novel functional nanostructured materials. *Adv. Mater.* 25(46):6672–90
27. Gopakumar TG, Lee JA, Kontopoulou M, Parent JS. 2002. Influence of clay exfoliation on the physical properties of montmorillonite/polyethylene composites. *Polymer* 43(20):5483–91
28. Jouault N, Vallat P, Dalmas F, Said S, Jestin J, Boueé F. 2009. Well-dispersed fractal aggregates as filler in polymer–silica nanocomposites: long-range effects in rheology. *Macromolecules* 42(6):2031–40
29. Novak BM. 1993. Hybrid nanocomposite materials—between inorganic glasses and organic polymers. *Adv. Mater.* 5(6):422–33
30. Qiang Y, Manohar N, Stebe KJ, Lee D. 2018. Polymer blend-filled nanoparticle films: via monomer-driven infiltration of polymer and photopolymerization. *Mol. Syst. Des. Eng.* 3:96–102
31. Srivastava S, Kotov NA. 2008. Composite layer-by-layer (LBL) assembly with inorganic nanoparticles and nanowires. *Acc. Chem. Res.* 41(12):1831–41
32. Kulkarni DD, Choi I, Singamaneni SS, Tsukruk VV. 2010. Graphene oxide–polyelectrolyte nanomembranes. *ACS Nano* 4(8):4667–76
33. Zhu Y, Wang H, Yan L, Wang R, Zhu Y. 2016. Preparation and tribological properties of 3D network polymer-based nanocomposites reinforced by carbon nanofibers. *Wear* 356:101–9
34. Wu Y, Ye K, Liu Z, Wang M, Chee KWA, et al. 2018. Effective thermal transport highway construction within dielectric polymer composites via a vacuum-assisted infiltration method. *J. Mater. Chem. C* 6(24):6494–501

35. Alshammary B, Walsh FC, Herrasti P, Ponce de Leon C. 2016. Electrodeposited conductive polymers for controlled drug release: polypyrrole. *J. Solid State Electrochem.* 20(4):839–59
36. Nejati S, Lau KKS. 2011. Pore filling of nanostructured electrodes in dye sensitized solar cells by initiated chemical vapor deposition. *Nano Lett.* 11(2):419–23
37. Bradford PD, Wang X, Zhao H, Maria JP, Jia Q, Zhu YT. 2010. A novel approach to fabricate high volume fraction nanocomposites with long aligned carbon nanotubes. *Compos. Sci. Technol.* 70(13):1980–85
38. Huang YR, Jiang Y, Hor JL, Gupta R, Zhang L, et al. 2015. Polymer nanocomposite films with extremely high nanoparticle loadings via capillary rise infiltration (CaRI). *Nanoscale* 7(2):798–805
39. Hor JL, Jiang Y, Ring DJ, Riggleman RA, Turner KT, Lee D. 2017. Nanoporous polymer-infiltrated nanoparticle films with uniform or graded porosity via undersaturated capillary rise infiltration. *ACS Nano* 11(3):3229–36
40. Venkatesh RB, Han SH, Lee D. 2019. Patterning polymer-filled nanoparticle films via leaching-enabled capillary rise infiltration (LeCaRI). *Nanoscale Horizons* 4(4):933–39
41. Venkatesh RB, Zhang T, Manohar N, Stebe KJ, Riggleman RA, Lee D. 2020. Effect of polymer-nanoparticle interactions on solvent-driven infiltration of polymer (SIP) into nanoparticle packings: a molecular dynamics study. *Mol. Syst. Des. Eng.* 5(3):666–74
42. Manohar N, Stebe KJ, Lee D. 2017. Solvent-driven infiltration of polymer (SIP) into nanoparticle packings. *ACS Macro Lett.* 6(10):1104–8
43. Manohar N, Stebe KJ, Lee D. 2020. Effect of confinement on solvent-driven infiltration of the polymer into nanoparticle packings. *Macromolecules* 53(15):6740–46
44. Bertei A, Nucci B, Nicolella C. 2013. Effective transport properties in random packings of spheres and agglomerates. *Chem. Eng. Trans.* 32:1531–36
45. Shin K, Obukhov S, Chen JT, Huh J, Hwang Y, et al. 2007. Enhanced mobility of confined polymers. *Nat. Mater.* 6(12):961–65
46. Yao Y, Butt HJ, Zhou J, Doi M, Floudas G. 2018. Capillary imbibition of polymer mixtures in nanopores. *Macromolecules* 51(8):3059–65
47. Yao Y, Alexandris S, Henrich F, Auernhammer G, Steinhart M, et al. 2017. Complex dynamics of capillary imbibition of poly(ethylene oxide) melts in nanoporous alumina. *J. Chem. Phys.* 146(20):203320
48. Martín J, Nogales A, Martín-González M. 2013. The smectic-isotropic transition of P3HT determines the formation of nanowires or nanotubes into porous templates. *Macromolecules* 46(4):1477–83
49. Whiteside PJD, Chininis JA, Hunt HK. 2016. Techniques and challenges for characterizing metal thin films with applications in photonics. *Coatings* 6(3):35
50. Campoy-Quiles M, Alonso MI, Bradley DDC, Richter LJ. 2014. Advanced ellipsometric characterization of conjugated polymer films. *Adv. Funct. Mater.* 24(15):2116–34
51. Hor JL, Wang H, Fakhraai Z, Lee D. 2018. Effects of polymer-nanoparticle interactions on the viscosity of unentangled polymers under extreme nanoconfinement during capillary rise infiltration. *Soft Matter* 14(13):2438–46
52. Hor JL, Wang H, Fakhraai Z, Lee D. 2018. Effect of physical nanoconfinement on the viscosity of unentangled polymers during capillary rise infiltration. *Macromolecules* 51(14):5069–78
53. Washburn EW. 1921. The dynamics of capillary flow. *Phys. Rev.* 17(3):273–83
54. Dimitrov DI, Milchev A, Binder K. 2007. Capillary rise in nanopores: molecular dynamics evidence for the Lucas-Washburn equation. *Phys. Rev. Lett.* 99(5):054501
55. Zhmud BV, Tiberg F, Hallstensson K. 2000. Dynamics of capillary rise. *J. Colloid Interface Sci.* 228(2):263–69
56. Kimmich R, Fatkullin N, Mattea C, Fischer E. 2005. Polymer chain dynamics under nanoscopic confinements. *Magn. Reson. Imaging* 23(2):191–96
57. Mangal R, Srivastava S, Archer LA. 2015. Phase stability and dynamics of entangled polymer-nanoparticle composites. *Nat. Commun.* 6:7198
58. Tu CH, Steinhart M, Butt HJ, Floudas G. 2019. *In situ* monitoring of the imbibition of poly(*n*-butyl methacrylates) in nanoporous alumina by dielectric spectroscopy. *Macromolecules* 52(21):8167–76
59. Keddie JL, Jones RAL, Cory RA. 1994. Size-dependent depression of the glass transition temperature in polymer films. *EPL* 27:59–64

60. Choi J, Clarke N, Winey KI, Composto RJ. 2014. Fast polymer diffusion through nanocomposites with anisotropic particles. *ACS Macro Lett*. 3(9):886–91
61. Tarnacka M, Talik A, Kamińska E, Geppert-Rybczyńska M, Kaminski K, Paluch M. 2019. The impact of molecular weight on the behavior of poly(propylene glycol) derivatives confined within alumina templates. *Macromolecules* 52(9):3516–29
62. Ediger MD, Forrest JA. 2014. Dynamics near free surfaces and the glass transition in thin polymer films: a view to the future. *Macromolecules* 47(2):471–78
63. Schneider GJ, Nusser K, Willner L, Falus P, Richter D. 2011. Dynamics of entangled chains in polymer nanocomposites. *Macromolecules* 44(15):5857–60
64. Lange F, Judeinstein P, Franz C, Hartmann-Azanza B, Ok S, et al. 2015. Large-scale diffusion of entangled polymers along nanochannels. *ACS Macro Lett*. 4(5):561–65
65. Roth C, Dutcher J. 2004. Mobility on different length scales in thin polymer films. In *Soft Materials*, ed. JR Dutcher, AG Marangoni, pp. 1–38. Boca Raton, FL: CRC Press. 1st ed.
66. Choi J, Hore MJA, Meth JS, Clarke N, Winey KI, Composto RJ. 2013. Universal scaling of polymer diffusion in nanocomposites. *ACS Macro Lett*. 2(6):485–90
67. Askar S, Wei T, Tan AW, Torkelson JM. 2017. Molecular weight dependence of the intrinsic size effect on T_g in AAO template-supported polymer nanorods: a DSC study. *J. Chem. Phys.* 146(20):203323
68. Schneider GJ. 2017. Dynamics of nanocomposites. *Curr. Opin. Chem. Eng.* 16:65–77
69. Gam S, Meth JS, Zane SG, Chi C, Wood BA, et al. 2011. Macromolecular diffusion in a crowded polymer nanocomposite. *Macromolecules* 44(9):3494–501
70. Bocquet L. 2020. Nanofluidics coming of age. *Nat. Mater.* 19(3):254–56
71. Frank B, Gast AP, Russell TP, Brown HR, Hawker C. 1996. Polymer mobility in thin films. *Macromolecules* 29(20):6531–34
72. Bansal A, Yang H, Li C, Cho K, Benicewicz BC, et al. 2005. Quantitative equivalence between polymer nanocomposites and thin polymer films. *Nat. Mater.* 4(9):693–98
73. Ring DJ, Riggleman RA, Lee D. 2019. Critical contact angle to induce capillary rise of polymers in nanopores does not depend on chain length. *ACS Macro Lett*. 8(1):31–35
74. Jin S, McKenna GB. 2020. Effect of nanoconfinement on polymer chain dynamics. *Macromolecules* 53(22):10212–16
75. Muthukumar M. 1991. Entropic barrier model for polymer diffusion in concentrated polymer solutions and random media. *J. Non-Cryst. Solids* 131–133(2):654–66
76. Lin CC, Gam S, Meth JS, Clarke N, Winey KI, Composto RJ. 2013. Do attractive polymer-nanoparticle interactions retard polymer diffusion in nanocomposites? *Macromolecules* 46(11):4502–9
77. Tung WS, Griffin PJ, Meth JS, Clarke N, Composto RJ, Winey KI. 2016. Temperature-dependent suppression of polymer diffusion in polymer nanocomposites. *ACS Macro Lett*. 5(6):735–39
78. Wang H, Hor JL, Zhang Y, Liu T, Lee D, Fakhraai Z. 2018. Dramatic increase in polymer glass transition temperature under extreme nanoconfinement in weakly interacting nanoparticle films. *ACS Nano* 12(6):5580–87
79. Forrest JA, Dalnoki-Veress K, Stevens JR, Dutcher JR. 1996. Effect of free surfaces on the glass transition temperature of thin polymer films. *Phys. Rev. Lett.* 77(10):2002–5
80. Keddie JL, Jones RAL. 1995. Glass transition behavior in ultra-thin polystyrene films. *Isr. J. Chem.* 35(1):21–26
81. Serghei A, Huth H, Schick C, Kremer F. 2008. Glassy dynamics in thin polymer layers having a free upper interface. *Macromolecules* 41(10):3636–39
82. Wang H, Qiang Y, Shamsabadi AA, Mazumder P, Turner KT, et al. 2019. Thermal degradation of polystyrene under extreme nanoconfinement. *ACS Macro Lett*. 8(11):1413–18
83. Glasmästar K, Gold J, Andersson A-S, Sutherland DS, Kasemo B. 2003. Silicone transfer during microcontact printing. *Langmuir* 19(13):5475–83
84. Millet L, Jain A, Gillette M. 2017. Less is more: Oligomer extraction and hydrothermal annealing increase PDMS bonding forces for new microfluidics assembly and for biological studies. bioRxiv 150953. **https://doi.org/10.1101/150953**
85. Sanchez W, Evans J, George G. 2005. Silicone polymers in scar remediation: the role of migration of oligomers through stratum corneum. *Aust. J. Chem.* 58(6):447–50

86. Hourlier-Fargette A, Dervaux J, Antkowiak A, Neukirch S. 2018. Extraction of silicone uncrosslinked chains at air-water-polydimethylsiloxane triple lines. *Langmuir* 34(41):12244–50
87. Berthier E, Young EWK, Beebe D. 2012. Engineers are from PDMS-land, biologists are from Polystyrenia. *Lab Chip* 12(7):1224–37
88. Kim JH, Hwang HS, Hahm SW, Khang DY. 2010. Hydrophobically recovered and contact printed siloxane oligomers for general-purpose surface patterning. *Langmuir* 26(15):13015–19
89. Gemici Z, Schwachulla PI, Williamson EH, Rubner MF, Cohen RE. 2009. Targeted functionalization of nanoparticle thin films via capillary condensation. *Nano Lett.* 9(3):1064–70
90. Kim BQ, Qiang Y, Turner KT, Choi SQ, Lee D. 2020. Heterostructured polymer-infiltrated nanoparticle films with cavities via capillary rise infiltration. *Adv. Mater. Interfaces* 8(3):2001421
91. Teraoka I, Langley KH, Karasz FE. 1993. Diffusion of polystyrene in controlled pore glasses: transition from the dilute to the semidilute regime. *Macromolecules* 26(2):287–97
92. Bishop MT, Langley KH, Karasz FE. 1989. Dynamic light-scattering studies of polymer diffusion in porous materials: linear polystyrene in porous glass. *Macromolecules* 22(3):1220–31
93. Park JY, McKenna GB. 2000. Size and confinement effects on the glass transition behavior of polystyrene/*o*-terphenyl polymer solutions. *Phys. Rev. B* 61(10):6667–76
94. Bezrukov SM, Vodyanoy I, Brutyan RA, Kasianowicz JJ. 1996. Dynamics and free energy of polymers partitioning into a nanoscale pore. *Macromolecules* 29(26):8517–22
95. Byrne MT, McCarthy JE, Bent M, Blake R, Gun'ko YK, et al. 2007. Chemical functionalisation of titania nanotubes and their utilisation for the fabrication of reinforced polystyrene composites. *J. Mater. Chem.* 17(22):2351–58
96. Selvin TP, Kuruvilla J, Sabu T. 2004. Mechanical properties of titanium dioxide-filled polystyrene microcomposites. *Mater. Lett.* 58(3–4):281–89
97. Thomas SP, Thomas S, Bandyopadhyay S. 2009. Mechanical, atomic force microscopy and focused ion beam studies of isotactic polystyrene/titanium dioxide composites. *Composites A* 40(1):36–44
98. Zhang J, Wang X, Lu L, Li D, Yang X. 2003. Preparation and performance of high-impact polystyrene (HIPS)/nano-TiO_2 nanocomposites. *J. Appl. Polym. Sci.* 87(3):381–85
99. Lin EY, Frischknecht AL, Riggleman RA. 2020. Origin of mechanical enhancement in polymer nanoparticle (NP) composites with ultrahigh NP loading. *Macromolecules* 53(8):2976–82
100. Jiang Y, Hor JL, Lee D, Turner KT. 2018. Toughening nanoparticle films via polymer infiltration and confinement. *ACS Appl. Mater. Interfaces* 10(50):44011–17
101. Ast J, Ghidelli M, Durst K, Göken M, Sebastiani M, Korsunsky AM. 2019. A review of experimental approaches to fracture toughness evaluation at the micro-scale. *Mater. Des.* 173:107762
102. Jancar J, Douglas JF, Starr FW, Kumar SK, Cassagnau P, et al. 2010. Current issues in research on structure-property relationships in polymer nanocomposites. *Polymer* 51(15):3321–43
103. Kumar SK, Benicewicz BC, Vaia RA, Winey KI. 2017. 50th anniversary perspective: Are polymer nanocomposites practical for applications? *Macromolecules* 50(3):714–31
104. Donovan BF, Warzoha RJ, Venkatesh RB, Vu NT, Wallen J, Lee D. 2019. Elimination of extreme boundary scattering via polymer thermal bridging in silica nanoparticle packings: implications for thermal management. *ACS Appl. Nano Mater.* 2(10):6662–69
105. Tran HH, Venkatesh RB, Kim Y, Lee D, Riassetto D. 2019. Multifunctional composite films with vertically aligned ZnO nanowires by leaching-enabled capillary rise infiltration. *Nanoscale* 11(45):22099–107
106. Zeng X, Xu S, Pi P, Cheng J, Wang L, et al. 2018. Polymer-infiltrated approach to produce robust and easy repairable superhydrophobic mesh for high-efficiency oil/water separation. *J. Mater. Sci.* 53(14):10554–68
107. Zhang J, Zhang L. 2019. Polystyrene/TiO_2 nanocomposite coatings to inhibit corrosion of aluminum alloy 2024-T3. *ACS Appl. Nano Mater.* 2(10):6368–77
108. Shavit A, Riggleman RA. 2015. The dynamics of unentangled polymers during capillary rise infiltration into a nanoparticle packing. *Soft Matter*. 11(42):8285–95